Space Weather

RESEARCH ARTICLE
10.1029/2026SW005032

Large, Long-Lasting Mid-Latitude Geomagnetically Induced Currents During a Moderate Geomagnetic Storm

A. W. Smith[1], C. J. Rodger[2], I. J. Rae[1], D. H. Mac Manus[2], M. A. Clilverd[3], J. Malone-Leigh[2], J. C. Coxon[1], C. D. Beggan[4], J. Hübert[4], A. Renton[5], A. P. Dimmock[6], C. Forsyth[7], M.-T. Walach[8], W. Sun[9], K. M. Pratscher[10], T. Petersen[10], and M. Dalzell[5]

[1]Department of Mathematics, Physics and Electrical Engineering, Northumbria University, Newcastle upon Tyne, UK, [2]Department of Physics, University of Otago, Dunedin, New Zealand, [3]British Antarctic Survey, Cambridge, UK, [4]British Geological Survey, Edinburgh, UK, [5]Transpower New Zealand Limited, Wellington, New Zealand, [6]Swedish Institute of Space Physics, Uppsala, Sweden, [7]Mullard Space Science Laboratory, University College London, Dorking, UK, [8]School of Physics and Astronomy, Lancaster University, Lancaster, UK, [9]Space Sciences Laboratory, University of California, Berkeley, CA, USA, [10]Department of Data Science and Geohazards Monitoring, Earth Sciences New Zealand, Lower Hutt, New Zealand

Key Points:

- A mid-latitude, steadily enhancing ionospheric current wedge had considerable, long-lasting (90 min) ground impact in the dawn sector
- This phenomena represents a hazard not well-captured by the typical proxy $\dot{H}$ (with a correlation of ~0.6)
- We highlight the limitations of relying upon geomagnetic indices, where mid-latitude events impact both ring current and auroral indices

Correspondence to:
A. W. Smith,
andy.w.smith@northumbria.ac.uk

Citation:
Smith, A. W., Rodger, C. J., Rae, I. J., Mac Manus, D. H., Clilverd, M. A., Malone-Leigh, J., et al. (2026). Large, long-lasting mid-latitude geomagnetically induced currents during a moderate geomagnetic storm. *Space Weather*, *24*, e2026SW005032. https://doi.org/10.1029/2026SW005032

Received 26 FEB 2026
Accepted 23 JUN 2026

Author Contributions:
Conceptualization: A. W. Smith, C. J. Rodger
Data curation: T. Petersen, M. Dalzell
Formal analysis: A. W. Smith, I. J. Rae, D. H. Mac Manus, M. A. Clilverd, J. Malone-Leigh, J. C. Coxon, C. D. Beggan, J. Hübert
Investigation: A. W. Smith, I. J. Rae, J. Malone-Leigh, C. D. Beggan, J. Hübert, A. Renton, A. P. Dimmock, C. Forsyth, M.-T. Walach, W. Sun, K. M. Pratscher
Methodology: C. J. Rodger, I. J. Rae, M. A. Clilverd, J. Malone-Leigh, K. M. Pratscher
Software: D. H. Mac Manus, M. A. Clilverd
Validation: C. J. Rodger, D. H. Mac Manus, M. A. Clilverd, J. C. Coxon, C. D. Beggan, J. Hübert, A. Renton, A. P. Dimmock, M.-T. Walach, K. M. Pratscher

Abstract Geomagnetically Induced Currents (GICs) are a key space weather hazard to ground-based infrastructure, and can cause mis-operation or even equipment failure. The solar wind interacts with the Earth's geomagnetic field, causing the magnetic field at ground level to vary with time. This variability causes GICs in grounded, conducting networks via coupling with the subsurface geology. Most studies of the hazard focus on short, high amplitude GICs, but long intervals of lower amplitude GIC can also be problematic, representing a rare but known pathway to equipment damage and power failure. We evaluate an interval in June 2015 where the power network in New Zealand experienced long-duration, steadily increasing GICs across the South Island. These GICs were up to 20A and lasted approximately 90 min during an otherwise moderate storm interval, while New Zealand was in the dawn sector. We investigate the magnetospheric cause, attributing them to a possible diversion of the ring current into the ionosphere. We test the ability of modeling and proxies to capture this hazard, finding that it can be recreated, but is dependent upon the regional geology, and requires detailed knowledge of the network configuration. We model two hypothetical examples, (a) where the magnetic perturbation is larger and (b) where a different mid-latitude location is exposed, finding that larger currents are possible and that the vulnerability is not unique to New Zealand. Our case study highlights the limitations of geomagnetic indices, which we show to be vulnerable to influence from such rare mid-latitude phenomena.

Plain Language Summary A key hazard of space weather is the generation of extra, quasi-DC currents within power networks, termed Geomagnetically Induced Currents (GICs). These anomalous GICs can cause problems with the safe, reliable operation of transformers in the power network–their study and mitigation require collaboration between academia and industry. In this event we show how an unusual current system in Earth's upper atmosphere posed a risk to mid-latitude locations, at a time of day that would normally not be considered to be at risk. The case study highlights a much less common mode of the hazard: a long interval of moderate GIC, as opposed to a short interval of very high current. We show that modern modeling is capable of capturing this behavior, but that the impact is highly dependent upon the local geology and requires precise knowledge of the power network topology as geographically close locations show distinct impacts. Critically, while historical case studies are important starting points, the precise threat depends on local geology and network topology. We also show that this type of event contaminates global measures of space weather (i.e., geomagnetic indices), on which many studies rely to quantify the severity of magnetospheric processes.

1. Introduction

An important space weather hazard is the generation of anomalous currents in grounded, conducting infrastructure such as high voltage power networks. Such anomalous currents are known as Geomagnetically Induced Currents (GICs). While inevitably always present at very low levels, GICs act as a DC offset in otherwise AC power networks. High levels of GIC can result in several different modes of transformer failure, resulting in outcomes from temporary disruption all the way through to permanent damage (Bolduc, 2002; Boteler, 2003; Dimmock et al., 2024; Kappenman, 2018; Molinski, 2002; Wallner et al., 2026). The cost of an extreme space weather event has been estimated to be of the order of tens of billions of dollars for a western economy

Visualization: A. W. Smith, J. Hübert, A. P. Dimmock
Writing – original draft: A. W. Smith
Writing – review & editing: C. J. Rodger, I. J. Rae, D. H. Mac Manus, M. A. Clilverd, J. Malone-Leigh, J. C. Coxon, C. D. Beggan, J. Hübert, A. Renton, A. P. Dimmock, C. Forsyth, M.-T. Walach, W. Sun, K. M. Pratscher, T. Petersen, M. Dalzell

(e.g., Eastwood et al., 2018; Oughton et al., 2019, 2025), a cost that can be reduced dramatically with sufficient forecasting and mitigation. This emphasizes the need to understand and predict hazardous space weather effects.

In the last few decades a range of magnetospheric phenomena have been empirically linked to problems with power network operation. The infamous Hydro Quebec power network failure in 1989 was inferred to be a result of a geomagnetic substorm during a geomagnetic storm (Bolduc, 2002; Boteler, 2019). Meanwhile, in 2001 New Zealand lost a power network transformer due to a GIC likely related to a contemporaneous Sudden Commencement (SC) (Beland & Small, 2004; Marshall et al., 2012). Later, in 2003 a series of power network problems in southern Sweden, including a blackout in Malmö, were attributed to the network configuration and magnetospheric phenomena including Sudden Commencements, substorms and enhanced ionospheric convection (Pulkkinen et al., 2005). More broadly, Rosenqvist et al. (2025) used a comprehensive list of Swedish power network disturbances to show that the disturbances are much more likely during strong (i.e., G4 and G5) geomagnetic storms. However, the hazard is very dependent upon location, local geology and specific network topology (e.g., Beggan et al., 2013; Dimmock et al., 2019; Parry et al., 2025).

Large GICs have long been considered more likely when large rates of change of the horizontal magnetic field are observed (H') (Bolduc et al., 1998; Viljanen et al., 2001). Physically, this corresponds to the chain of causality: a changing magnetic field induces a geoelectric field in the solid Earth that is then related to a GIC in the infrastructure in question. Indeed, a good empirical correlation has been observed between long duration GIC data sets and magnetic field data in New Zealand, both during intense H' "spikes" (e.g., Rodger et al., 2017), and the data as a whole (e.g., Mac Manus et al., 2017). Limiting the consideration from the range of magnetospheric processes that can cause elevated H' to specific phenomena has been shown to tighten this correlation further (A. W. Smith et al., 2022, 2024).

While alternative proxy measurements to H' have been developed (and often show excellent performance e.g., Marshall et al., 2011; Waters and Marshall, 2026), historically, studies examining the potential impact of extreme events often rely on H', which provides a convenient and widely available proxy (e.g., Fogg et al., 2023; Rogers et al., 2020, 2021; Thomson et al., 2011; Wang et al., 2025). Such extreme value analyses provide unique insight into what may be expected during 1 in 100 years events, for example. Correspondingly, there has been great interest in the last decade in forecasting H' (Iong et al., 2024; Keesee et al., 2020; Madsen et al., 2022; Pinto et al., 2022; Upendran et al., 2022), or whether it will exceed specific, high thresholds (Camporeale et al., 2020; Coughlan et al., 2023; A. W. Smith, Forsyth, Rae, Garton, et al., 2021). Meanwhile, statistical studies of large magnetic activity (i.e., H') have investigated the causal magnetospheric processes and their relative significance (e.g., Milan et al., 2023, 2024; Schillings et al., 2022). The most commonly attributed phenomena include substorms (Freeman et al., 2019), sudden commencements (A. W. Smith, Forsyth, Rae, Rodger, & Freeman, 2021; A. W. Smith et al., 2019), and auroral omega bands (Apatenkov et al., 2020; Hodnett et al., 2025). A high degree of regional variability, particularly during substorms and within the auroral zone, has been highlighted as a critical facet of the threat of space weather from large H' (Dimmock et al., 2020; Kärhä et al., 2023).

While the focus is often on understanding and predicting large, transient H' (e.g., "spikes") and associated GICs, a similar level of hazard to electrical equipment can be achieved through longer intervals of smaller currents, in addition to cumulative, long-term effects (Zois, 2013). For example, Mac Manus, Rodger, Dalzell, et al. (2022) detail limits that would present a risk of causing an excessive loss of transformer lifespan (greater than 20% loss), or an unacceptable chance of catastrophic failure. For a single phase bank transformer design the tolerable duration of 100 A is stated to be 15 min, while a lower level of 50 A could be tolerated for 120 min. Similar limits have been discussed for Swedish transformers (Rosenqvist et al., 2022). Enhanced and sustained GIC at relatively moderate levels leads to transformer cores becoming saturated, which produces harmonic distortion (Clilverd et al., 2018; Crack et al., 2024; Rodger et al., 2020). Such distortions are an additional route to power grid failure (Guillon et al., 2016; Schrijver et al., 2014), separate to the thermal issues which were the focus of the Mac Manus, Rodger, Ingham, et al. (2022) work. In the present case study we show an example in which a relatively moderate geomagnetic storm resulted in elevated GICs (~20 A) in transformers across New Zealand. Although these GICs were not by any means "extreme," they are long lasting, occur during a geomagnetic disturbance with relatively low H' levels, and built over the course of approximately 90 min. We examine the solar wind driving and magnetospheric processes active during the interval, as well as the implications for forecasting and modeling of such events.

2. Data

We use data from several different sources within this case study. For observations local to the power network, we show geomagnetic field data from the Eyrewell magnetic observatory (EYR, −50° MLat). These data are presented at a 1 minute resolution and were obtained from INTERMAGNET (GNS Science, 2022), in a geographic coordinate system (with X, Y and Z representing the North, East and vertical components). For complementary magnetic observations across the globe we turn to SuperMAG (Gjerloev, 2012). These data have a baseline removed and are provided in a geomagnetic coordinate system (with N, E, Z representing the North, East and Vertical components, respectively). We also present auroral electrojet and partial ring current indices, sourced from SuperMAG (Newell & Gjerloev, 2011, 2012).

We compare the EYR magnetic observatory data with the GIC data collected from four locations in the South Island of New Zealand. The method by which these data are collected and stored can be found in Mac Manus et al. (2017). We note that the time resolution of the data is variable, nominally 4 s, but with longer time gaps if the GIC values are changing by a small amount (e.g., < 0.2 A) (e.g., Clilverd et al., 2020). For the majority of the period of interest the GIC data is at 4 s resolution.

The ground-based measurements are supplemented by measurements of the field aligned currents (FACs), provided by the Active Magnetosphere and Planetary Electrodynamics Response Experiment (AMPERE). These FAC measurements are available from 2010, and are derived using the magnetometers onboard the Iridium Communication Network constellation (Anderson et al., 2000, 2021; Waters et al., 2001, 2020). We note that the AMPERE data are nominally provided at a 2 minute resolution, within a 10 min sliding window.

Complementing these terrestrial observations we use the OMNI data set (Papitashvili & King, 2020), from NASA/GSFC's OMNIWeb (https://omniweb.gsfc.nasa.gov/) for observations in the solar wind (propagated to Earth's bow shock) and for several geomagnetic indices and derived data products (e.g., the solar wind convection electric field: $-V_{SW}$ multiplied by B_Z^{GSM}). The magnetic field is used in the Geocentric Solar Magnetospheric coordinate system: the X-axis points toward the Sun, the Y-axis is defined by the cross product between the X-axis and the Earth's magnetic dipole (positive toward dusk), and the Z axis completes the right-handed set.

3. Case Study: Geomagnetic Storm June 2015

3.1. Storm Overview

The geomagnetic storm on 22 June 2015 was a large storm, but far weaker than the 1989 and 2003 extreme storms. When ranked by minimum Dst it was the 7th largest storm of 2015 (Minimum $Dst = -114$ nT within the period of focus), with a maximum Kp of 8+ (thereby a G4 storm). For context, NOAA SWPC (Space Weather Prediction Center) estimate that approximately 100 such storms occur during every 11 years solar cycle. Figure 1 shows the interplanetary conditions and ring current indices for a 4.5 hr period covering the key part of the geomagnetic storm. Five epochs (labeled α, β, γ, δ, and ϵ) are marked and will be used to outline the interval and subsequent interpretation.

While we focus on the defined 4.5 hr interval detailed in Figure 1, we note that the days around this period were active, with complex and sustained solar wind activity (Gopalswamy et al., 2018), and consequently the broader period has attracted study of its ionospheric (e.g., Macho et al., 2020) and wider geomagnetic impacts (e.g., Liu et al., 2016; Piersanti et al., 2017; Reiff et al., 2016). For context, prior to the plotted interval two weaker interplanetary shocks impacted the magnetosphere in the preceding ∼24 hour period. These may have preconditioned the magnetosphere. We also note that the storm intensified on the 23 June, subsequent parts of the magnetic cloud featured strong, extended periods of negative B_Z^{GSM} that leads to a more intense ring current with SMR reaching ∼− 200 nT. Appendix A and Figure A1 displays a broader time interval, with more discussion of the period in question.

Epoch α precedes the geomagnetic storm, with solar wind conditions being relatively inactive: B_Z^{GSM} is around zero, while the solar wind velocity is only moderately elevated at around 450 km s^{-1}. Epoch β is at the time of arrival of an interplanetary shock. The timing discrepancy between the OMNI-derived data (Figures 1a–1c) and the SYM-H response in Figure 1d is the result of the uncertainty from the OMNI propagation process. Nonetheless, the shock is large, with the solar wind velocity reaching ∼700 km s^{-1}. B_Z^{GSM} also turns moderately southward, dipping to approximately −15 nT.

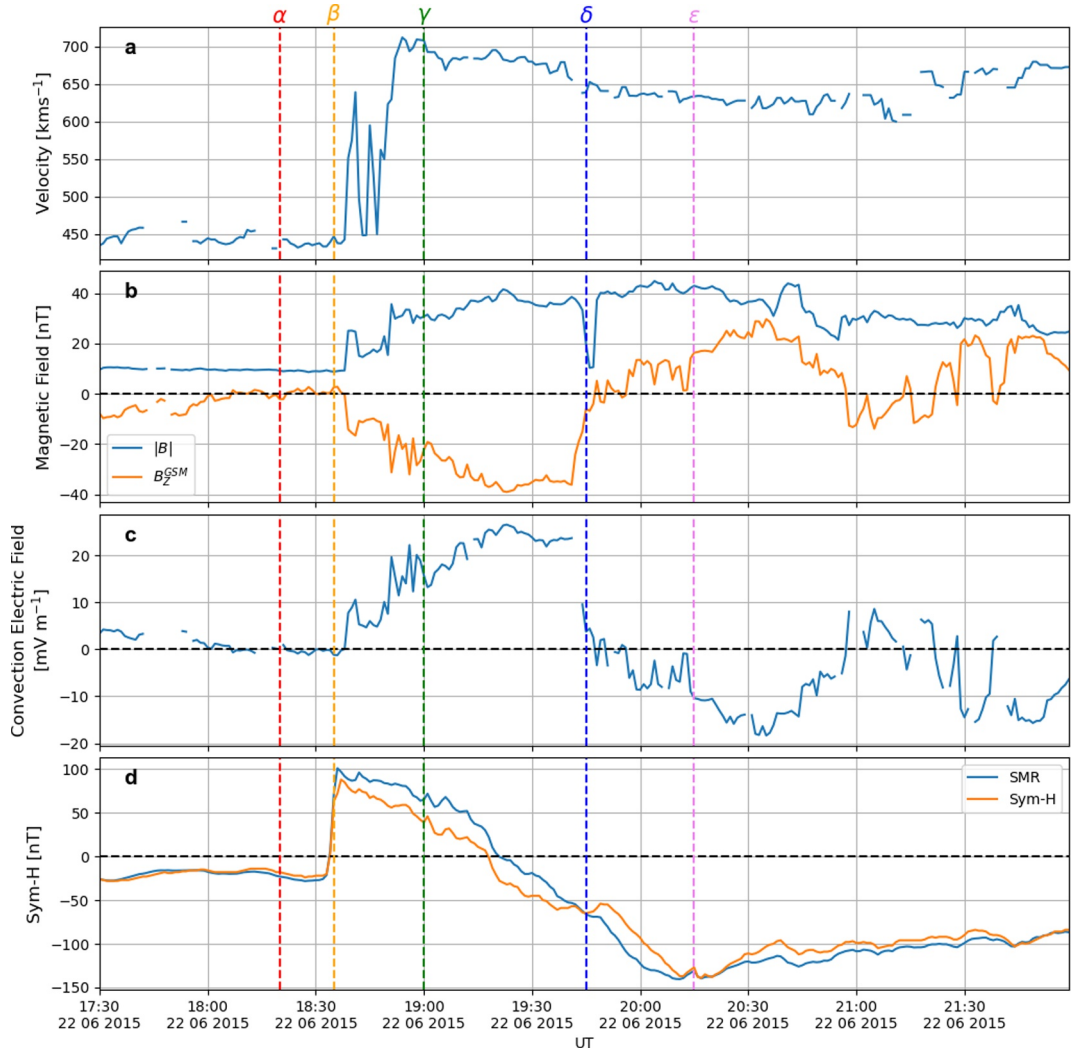

Figure 1. An overview of the solar wind and geomagnetic conditions during the 22 June 2015 geomagnetic storm. Panels (a–c) show the solar wind velocity, the interplanetary magnetic field strength ($|B|$) and north-south component of the magnetic field (B_Z^{GSM}), and convection electric field. Panel (d) shows the SYM-H and SMR ring current indices. Five epochs are marked (α, β, γ, δ, and ϵ) through the interval and will be referred to throughout the manuscript.

In the 70 min between epochs β and δ we see the interplanetary magnetic field (IMF) intensify, becoming more strongly southward with B_Z^{GSM} decreasing to ~ -40 nT. The solar wind velocity remains elevated, though reducing slightly. This combination results in a steady increase in the convection electric field. From a magnetospheric standpoint, if we take the SYM-H index as representing the ring current at this time in the storm, this interval appears to correspond to a steadily increasing ring current intensity. We do note a two-stage decrease in SYM-H, with a plateau around epoch δ, one that is not reproduced in SMR, an alternative ring current proxy. The storm main phase appears to complete at epoch ϵ, with SYM-H having declined between epochs δ and ϵ, but the IMF having rotated such that $B_Z^{GSM} \sim 0$.

3.2. New Zealand Geomagnetically Induced Currents

We now turn to the GICs measured in the New Zealand power network. Figure 2a shows the background-subtracted horizontal ground magnetic field (where $B_H = \sqrt{B_N^2 + B_E^2}$) as measured at the EYR magnetometer station, near Christchurch, New Zealand. The background is simply taken as the value at 17:30 UT. The rate

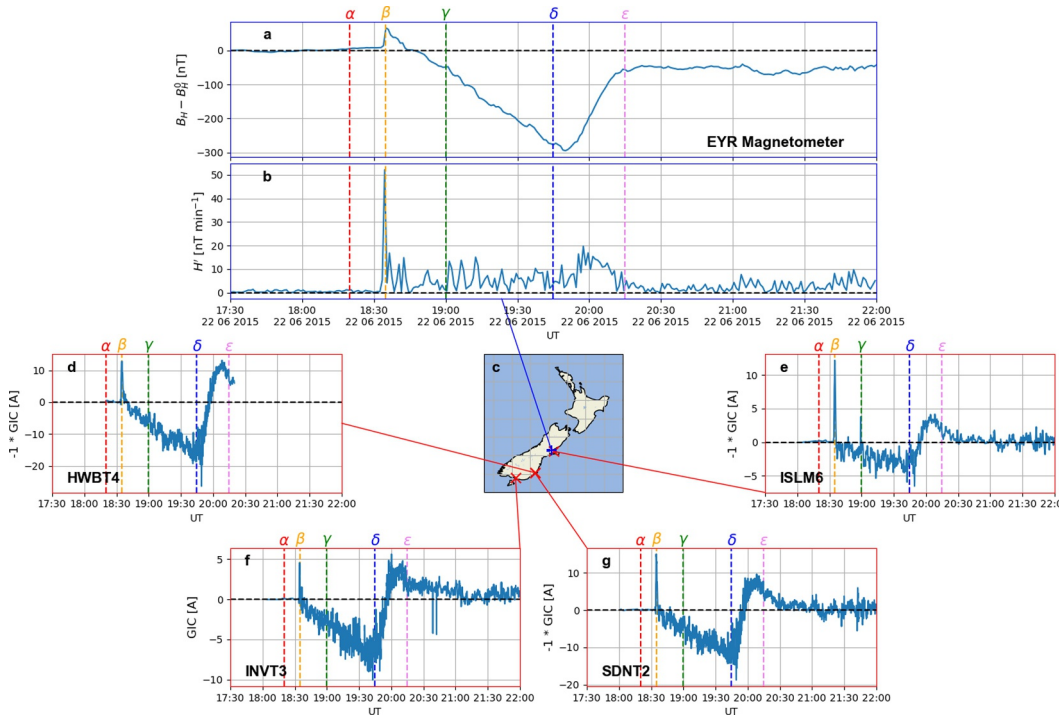

Figure 2. The ground impact of the 22 June 2015 geomagnetic storm in New Zealand. The horizontal geomagnetic field (and rate of change of the field) is shown in panels (a and b). A contextual map of New Zealand is provided in panel (c), while the Geomagnetically Induced Current measured at four locations across the South Island are then shown in panels (d–g). As in Figure 1, five epochs (α, β, γ, δ, and ϵ) are indicated throughout the storm.

of change of the horizontal field (H') is shown in Figure 2b. The first signature of the storm here is the SC at epoch β, clear as an increase in B_H and a spike in H'.

For the remaining storm main phase (i.e., between epochs β and ϵ) we see a slow decrease in B_H over approximately 70 min (to epoch δ), after which B_H increases back toward the background level in ∼30 minutes (to epoch ϵ). We also see elevated activity in H' but nothing approaching the level of the Sudden Commencement (SC, $\sim 50\,\mathrm{nT\ min^{-1}}$). The lower level of activity is mostly sporadic, but of the order of $\sim 5 - 15\,\mathrm{nT\ min^{-1}}$.

Figures 2d–2g show the GIC recorded at four transformers across the South Island of New Zealand. The sign of the GIC has been rectified such that it is consistent with the sign of the B_H change. We see the same pattern of response in all four locations, but with differing magnitudes. At all locations we first see the SC-related GIC spike at epoch β. The magnitude of this peak GIC is between 4 and 15 A, depending on location. Following the SC-related GIC spike we then see a similar pattern to that displayed in Figure 2a (i.e., B_H). We see a ramp-like increase in the magnitude of GIC for approximately 70 min before it peaks and reverses, with a smaller secondary peak of the opposite sign just before epoch ϵ. The GIC "ramp" increases at all locations to an absolute maximum GIC of between 5 and 20 A, in three out of four locations exceeding that observed during the SC itself, the exception being ISL M6 (near Christchurch and the EYR magnetometer, Figure 2e). This GIC "ramp" represents an unexpectedly long duration, widespread and relatively intense GIC. Without inspection of the full time-series, the peak GIC value itself would be easy to dismiss, but as highlighted by Mac Manus, Rodger, Dalzell, et al. (2022) a long duration of a less intense GIC can be as hazardous as a larger, shorter spike.

3.3. Magnetospheric Activity

The solar wind driving during this storm is undoubtedly elevated, but on first inspection Figure 1 did not appear particularly dramatic. We now examine the magnetospheric processes active during the interval to gain insights into why the abnormal ground geomagnetic response in New Zealand occurred. For this purpose, Figure 3 principally shows a selection of geomagnetic indices.

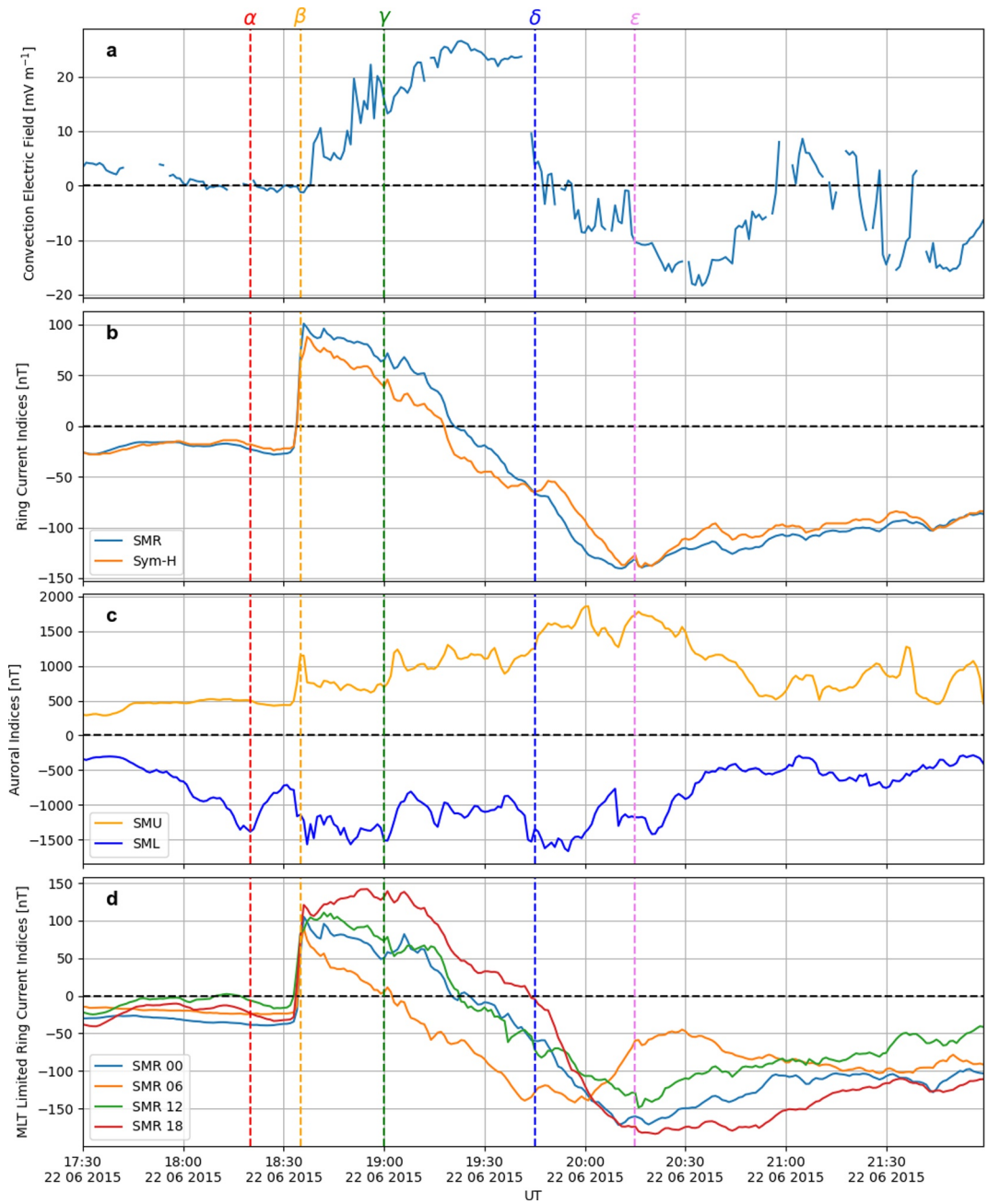

Figure 3. The geomagnetic conditions during the 22 June 2015 geomagnetic storm. The panels detail the solar wind convection electric field (a), selected ring current indices (b), SuperMAG auroral indices (c), and SuperMAG partial ring current indices (d). As above, five epochs are marked (α, β, γ, δ, and ϵ) throughout the storm.

Figure 3a shows the convection electric field, reproduced from Figure 1c. We again note the steady increase between epochs β and δ, associated with the high solar wind velocity and increasingly strong (and Southward) IMF. The ring current indices (SYM-H and SMR) are shown in Figure 3b, and both show what appears to be a fairly typical geomagnetic storm, with what we may infer to be a steadily increasing ring current between epochs β and ϵ. Meanwhile, the SuperMAG auroral indices (SML and SMU) are elevated during the interval, though without clear, definitive substorm-like morphology in SML (c.f., Forsyth et al., 2015; Lao et al., 2025), but convection is likely strong due to the strongly negative B_Z^{GSM} (Figure 1). The enhanced bay in SML throughout the storm (e.g., between epochs β and ϵ) would appear to indicate enhanced nightside convection, perhaps a steady magnetospheric convection (SMC) event (e.g., Walach et al., 2017; Walach & Milan, 2015).

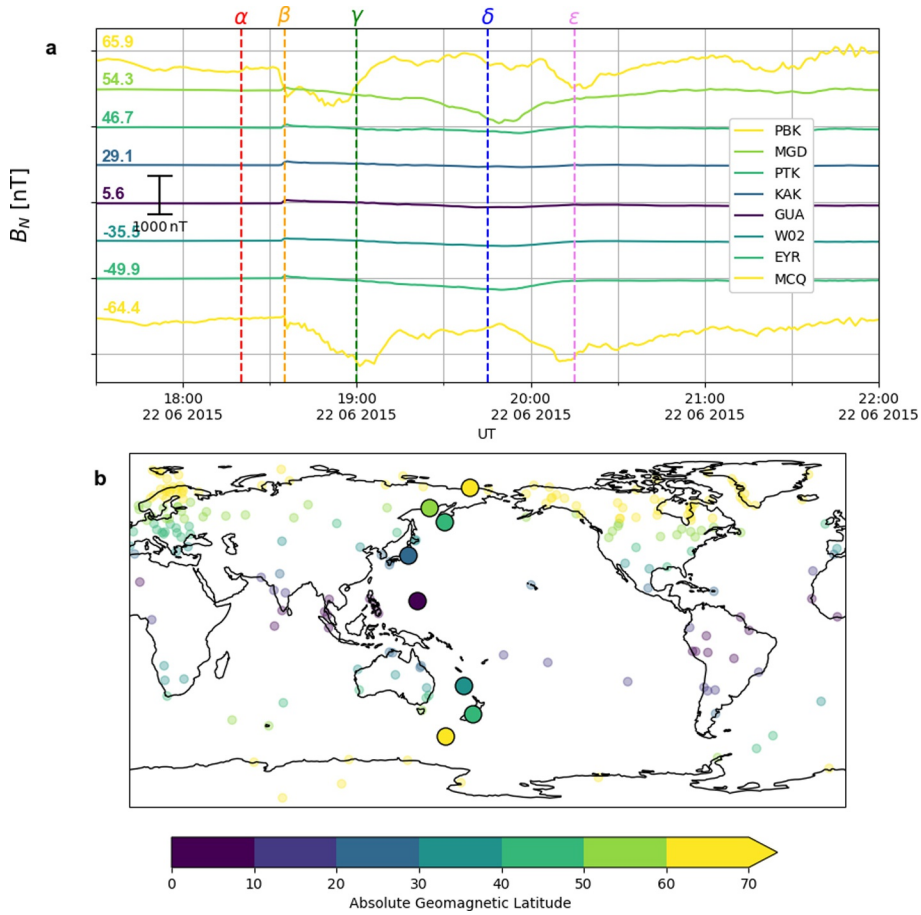

Figure 4. Time-series of the B_N component of the magnetic field observed by eight magnetometer stations (a). The time-series are ordered in latitude, with a fixed 1,000 nT offset between each time series. The data are color-coded by the absolute geomagnetic latitude of the magnetic observatory. Below, (b) a map where the stations plotted in (a) are denoted with large circles, other SuperMAG observatories are indicated with translucent dots.

We note here that while we have shown Southern hemisphere impact (i.e., in New Zealand, Figure 2), the majority of the data that constructs the indices in Figures 3b–3d is from the Northern hemisphere, due to geographical sampling and choices in the index derivation. Any North-South asymmetry (c.f. Coxon et al., 2016) would impact conclusions drawn from such data sets, though we note that we are mostly concerned with large, long time scale perturbations rather than precise timing or magnitudes. We will return to this consideration throughout our interpretation.

Figure 3d shows the SuperMAG partial ring current indices, with the SMR index in Figure 3b effectively broken down by magnetic local time. Within the main phase of a storm SMR18 is expected to drop fastest and furthest (Newell & Gjerloev, 2012), representing the injection of protons into the ring current in this local time region (i.e., 18 MLT). However, we can clearly see here that SMR06, representing the dawn segment (i.e., 6 MLT), decreases first and fastest (at epoch β) before being followed by SMR00 and SMR12. It is only at epoch δ where SMR18 drops rapidly, before peaking at (or just after) epoch ϵ. We note that SMR06 represents a similar morphology between epochs β and δ to the horizontal ground magnetic field signature observed in EYR in Figure 2a, which can be readily understood given the dawn-adjacent location of EYR at this time.

To investigate this further, we examine the magnetic field observations made within the dawn region during this storm. Figure 4a shows time-series of the B_N (North–South) magnetic field component observed by eight observatories, covering as full a range of magnetic latitudes as possible. Above an absolute geomagnetic latitude of 60° we see clear evidence of two magnetic depressions, with B_N minima around epochs γ and ϵ. This is approximately consistent between the hemispheres (i.e., at PBK and MCQ). Meanwhile at the lowest latitude

station (GUA, magnetic latitude of 5.6°) we see the classic signature expected during a geomagnetic storm, the early rise (epoch α) of the SC and gradual strengthening of the ring current (up to epoch δ). The classic ring current signature appears to reduce in magnitude with increasing latitude (i.e., moving to KAK and W02 at absolute geomagnetic latitudes of 29° and 35° respectively), as expected with increasing distance from the ring current.

However, at the mid-latitude stations: MGD, PTK and EYR, we see something unexpected. MGD, PTK and EYR are located at absolute geomagnetic latitudes of 54°, 47°, and 50°, respectively, and span both hemispheres. Both MGD and EYR show what appears to be an enhanced "ring current-like" signature compared to lower latitudes, with a steady decrease in B_N between epochs β and δ. We note that while a decreasing B_N may be attributed to a ring current (though typically maximizing at low latitudes), it would also be consistent with an increasing ionospheric current wedge (e.g., A. J. Smith et al., 2002). In the Northern hemisphere (MGD and PTK) there appears to be almost a two-step change, with two different slopes, an initial gentle decline that pauses after epoch γ before reducing at a faster rate. In comparison, EYR shows a much more smooth, consistent reduction in B_N between epochs β and δ. Though the sampling between the hemispheres is not equivalent in latitude, but is approximately consistent with a symmetrical signature.

If we compare these local observations to the geomagnetic indices shown in Figure 3, we can begin to understand the non-standard storm presentation (e.g., progression in partial ring current indices in Figure 3d). The SMR index is constructed from the data collected by 98 stations at mid and low latitudes (i.e., below 50° geomagnetic latitude, covering both hemispheres). This compares to six stations (from a collection of 10 possible options) for SYM-H (or four for Dst) (Newell & Gjerloev, 2012). Similarly to SMR, all stations that could contribute to SYM-H are at or below an absolute geomagnetic latitude of 50° (Iyemori, 1990). Therefore, any mid-latitude geomagnetic disturbance impacting stations such as PTK or EYR may well be reproduced in "ring current" indices. This therefore may explain the similarity between the PTK observations and the SYM-H index, with their two-stage decrease, noted in previous discussion of Figure 1d. SMR appears to be more robust to this, perhaps due to the greater number of stations contributing to its derivation, which may average out a mid-latitude geomagnetic disturbance that is limited in longitude.

Similarly, the SML and SMU indices amalgamate around 100 magnetometer locations, between 40° and 80° geomagnetic latitude (Newell & Gjerloev, 2011). In Figure 3c SML and SMU appeared broadly enhanced in this interval, attesting to strong current flowing in the auroral regions, but with relatively few defined features that may be used to identify substorm-like activity (c.f., Forsyth et al., 2015). On inspection of Figure 4, we see that above a latitude of $\sim$60° two clear depressions of B_N become apparent, peaking in magnitude around epochs γ and ϵ. In between these two epochs, a magnetospheric disturbance at mid latitudes (i.e., $\sim$50°) will be amalgamated by such auroral indices by virtue of the stations' inclusion within the set (i.e., 40° < MLat < 80°).

3.4. The Mid-Latitude Geomagnetic Disturbance

We now examine the nature of the geomagnetic disturbance in more detail, primarily using the full SuperMAG array of magnetometers in the mid and high latitude Northern hemisphere, due to superior spatial coverage as compared to the Southern hemisphere. Figure 5 shows the distribution of geomagnetic disturbances (white outlined points for each SuperMAG observatory, with the left and middle columns of Figure 5 representing the B_N and B_E components respectively. The right-hand column shows the northern hemisphere FACs, as inferred from AMPERE, to compare with the commensurate ground-based observations. The southern hemisphere AMPERE data can be found in Appendix B, where Figure B1 displays both hemispheres in an equivalent format to Figure 5. Each row of Figure 5 represents one of the five key epochs (α, β, γ, δ, and ϵ). In the left and middle columns, the background color represents an RBF (radial basis function) interpolation of the SuperMAG station level data (with a Gaussian kernel, performed in a Cartesian geomagnetic coordinate system) designed to ease interpretation.

First, in Figure 5a (epoch α) we see background, relatively quiescent magnetic signatures, with moderate values of B_N and B_E (after the SuperMAG baseline has been subtracted). The FACs are located at high latitudes, above $\sim|60°|$. Figure 5b (epoch β) then shows the impact of the interplanetary shock. This acts to enhance the previous magnetometer observations, along with a general positive northward (B_N) change globally, indicated with the light red shading that is particularly clear at lower latitudes.

10.1029/2026SW005032

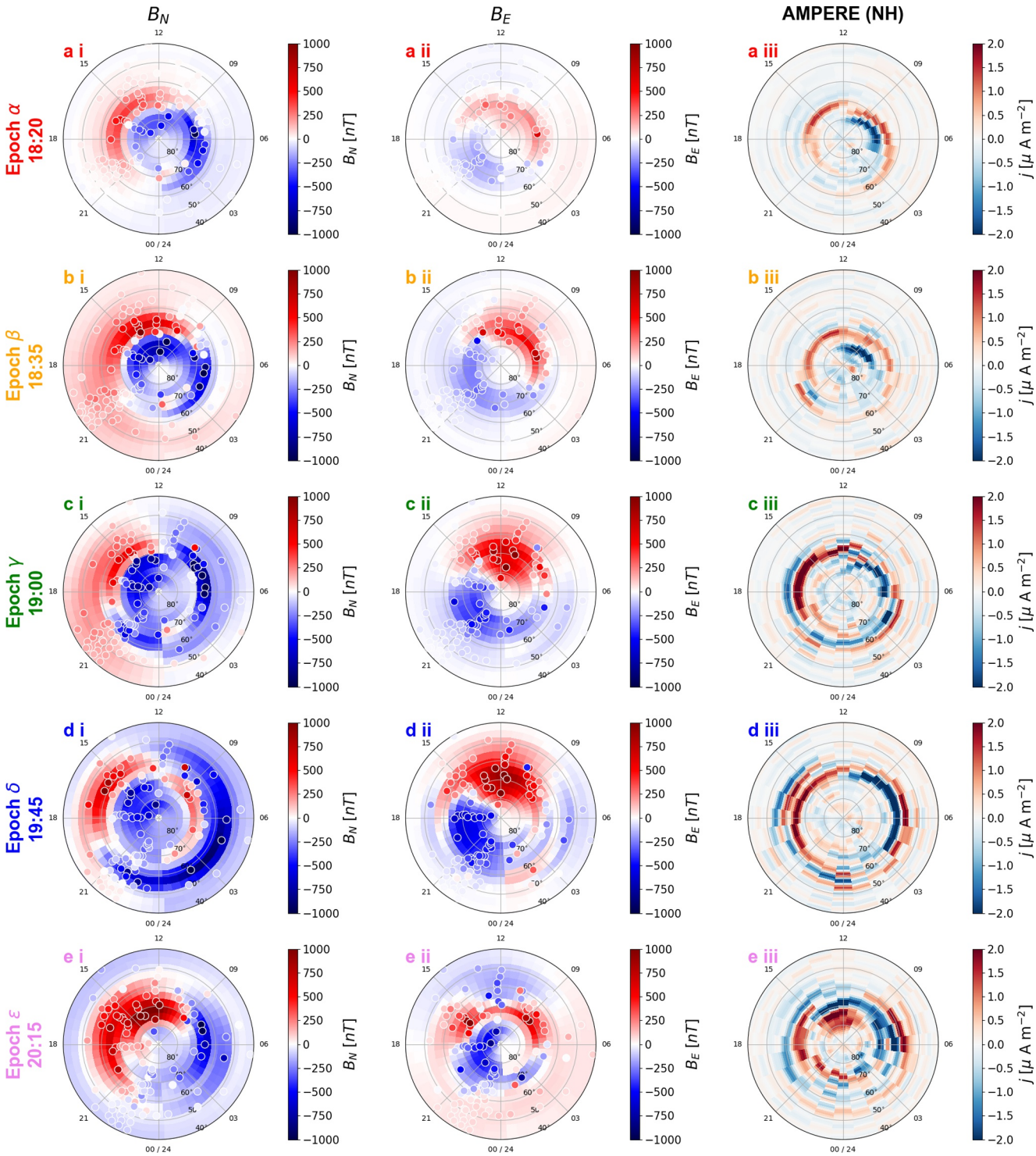

Figure 5. Geomagnetic polar plots displaying SuperMAG observations of the geomagnetic field (left and middle: i and ii) and Active Magnetosphere and Planetary Electrodynamics Response Experiment observations of the field aligned currents (right: iii) during the five key periods highlighted throughout the storm in the Northern hemisphere, down to a geomagnetic latitude of 40°. In the left and middle columns, the white-outlined dots represent the SuperMag locations, with the color representing B_N (left, column i) and B_E (right, column ii). The five epochs (α, β, γ, δ, and ϵ) in question represent the five rows in turn. In the left and middle columns the background color indicates interpolation of the SuperMAG data.

Figure 5c (epoch γ) then shows the ground magnetic field close to the peak of the magnetic signature of the first magnetic depression (derived from Figure 4a). Here we see a strong high latitude signature form in the dawn-sector, typified by the very low B_N that peaks around 65° magnetic latitude between 0500 and 0900 MLT. At this time the FACs in both the dawn and dusk regions are intensified, as compared to the previous epochs, and have expanded to slightly lower latitudes. This provides additional evidence that this could be a SMC event (e.g., Milan et al., 2017; Walach et al., 2017). As this is during Northern hemisphere summer, close to solstice, the terminator during this interval will extend beyond the pole. Therefore the strong B_N signatures could be related to the enhanced ionospheric conductivity and strong convection inferred at this time (e.g., Figure 1). Pre-midnight we may also see an intensification of B_N around 65° which could be a substorm-like current wedge.

Figure 5d (epoch δ) details the ground magnetic field at the peak of the identified "ramp-like" signature at mid-latitudes (i.e., EYR at ∼50°). In Figure 5di we see the fully formed mid-latitude current wedge (strong negative B_N), peaking around 55° and stretching broadly in local time, potentially from 2100 round to 1000 in the morning sector (though with relatively few observations in the dawn-noon region this is not definitive). The pre-midnight portion of the B_N signature is about 10° lower than any substorm-related current in epoch γ. We note that this places MGD nearly within the peak of this current system, and EYR toward the equatorward edge (in the conjugate Southern hemisphere, not shown). The FACs, as reported by AMPERE, are intense and have also moved to lower latitudes, about 10° lower than in epoch γ. The FACs indicate the ionospheric (rather than magnetospheric) origin of the strong B_N signature in the ground magnetic field.

Finally, Figure 5e (epoch ϵ) shows the end of the identified storm main phase, within the second high latitude magnetic depression in Figure 4a. The mid-latitude current system from 30 min prior (epoch δ) has dissipated, with a relatively localized high latitude current wedge (negative B_N, peaking around 70°) being present in the dawn sector, similar to epoch γ. At this time the FACs have faded at lower latitudes (i.e., circa 50°), and are located mostly at higher latitudes once more, but nonetheless are still intense relative to both pre-storm (epoch α) and the time of shock arrival (epoch β).

4. GIC Reproduction With Modeling

We now consider the capability of a typical GIC modeling process to capture the consequences of long-period magnetic activity, such as that described above. As shown in Figure 2, the observed H' is moderate, and on that basis alone any simple scaling or relation based solely upon those values (e.g., Mac Manus et al., 2017; Rodger et al., 2017; A. W. Smith et al., 2022) would underestimate the hazard in this interval.

We employ a thin sheet model of New Zealand that has been extensively used and validated (e.g., Divett et al., 2018, 2020; Mac Manus, Rodger, Dalzell, et al., 2022). The modeling approach is extensively discussed in Section 2 of Mac Manus, Rodger, Ingham, et al. (2022), but we reproduce the key details here. The ground geoelectric field is first calculated with a thin-sheet conductance model of New Zealand and the surrounding region (e.g., Vasseur & Weidelt, 1977). The empirical (integrated) conductance of the uppermost 20 km of crust are provided with a grid spacing of 1/6°. Below this depth, four layers are used with resistivities of 1,000, 10,000, 100 and 1 Ω/m with boundaries at depths of 20, 60, and 320 km (e.g., Figure 1 Mac Manus, Rodger, Ingham, et al., 2022). As input, the ground geomagnetic field is provided at a 1 minute cadence, with a resolution of 0.1 nT. The New Zealand AC power network consists of a large number of substations (∼190) often with multiple transformers (for a total of ∼590 transformers) covering three different voltages (50/66 kV, 110 kV, and 220 kV). Our method follows the approaches of Lehtinen and Pirjola (1985) and Boteler and Pirjola (2014) to represent the network at a transformer level (e.g., Divett et al., 2018, 2020).

Figure 6 details the results of applying the thin sheet model to the storm of June 2015. Figures 6a and 6b show the background subtracted B_X and B_Y components of the geomagnetic field. Figure 6c provides the geographical context as to where the observations correspond, and Figures 6d–6g show the observations and model results at the four locations from Figure 2. Figure 7 then shows two metrics evaluated at each of the four locations: (a) the Pearson correlation coefficient (r, Figure 7a) and the Prediction Efficacy ("P," Figure 7b) (e.g., Shim et al., 2011), based upon the root-mean-square error as suggested by Marsal and Torta (2019). Specifically, we define:

$$P = 1 - \left(\frac{\mathrm{RMSE}_{o,m}}{\sigma_o}\right) \quad (1)$$

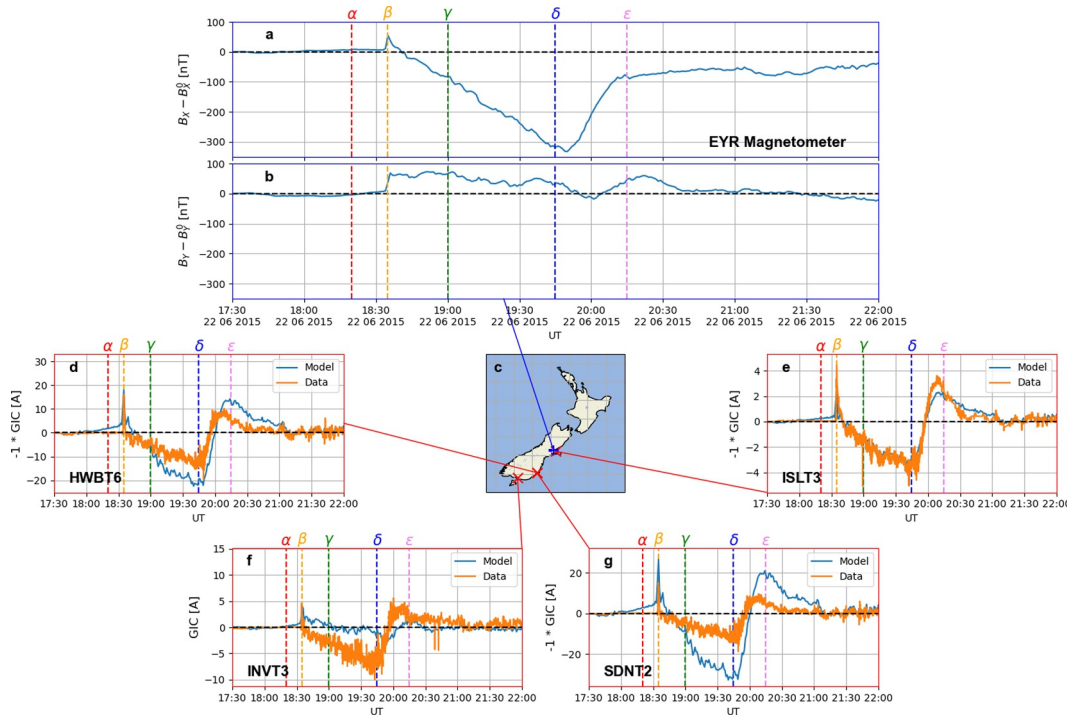

Figure 6. Modeling the ground impact in New Zealand with thin sheet modeling. Panels (a and b) show the background subtracted North and East components of the magnetic field recorded at EYR. A contextual map, with links to the other panels is shown in panel (c). Panels (d–g) show the modeled (blue) and observed (orange) Geomagnetically Induced Current (GIC) at four locations across the South Island. The sign of the GIC is arbitrary and has been matched to the orientation of the B_X variation shown in panel a for consistency. As above, five epochs (α, β, γ, δ, and ϵ) are marked throughout the storm.

where RMSE is the root-mean-square error between the model (m) and observations (o), and σ_o describes the standard deviation of the observations. This formulation is such that a score of 1 indicates perfect performance, 0 would be scored by a model simple equal to the mean of the observations ($RMSE = \sigma_o$), and anything less than zero indicates worse performance (Marsal & Torta, 2019; Shim et al., 2011). Combining the Pearson correlation and Prediction Efficacy (P) informs us as about the models ability to match pattern/shape and bias/error magnitude, respectively.

Figures 6a and 6b show that the main magnetic disturbance at this time is in the North-South orientation, with the field changing by several hundred nT between epochs β and δ. At Islington (ISL, Figure 6e), closest to the EYR magnetic observations, we see excellent correspondence between the GIC observations (orange) and model results (blue), capturing both the pattern ($r = 0.97$) and magnitude ($P = 0.73$) of the GIC. This clearly shows that the thin sheet modeling method is capable of replicating this form of event. As we consider locations to the South

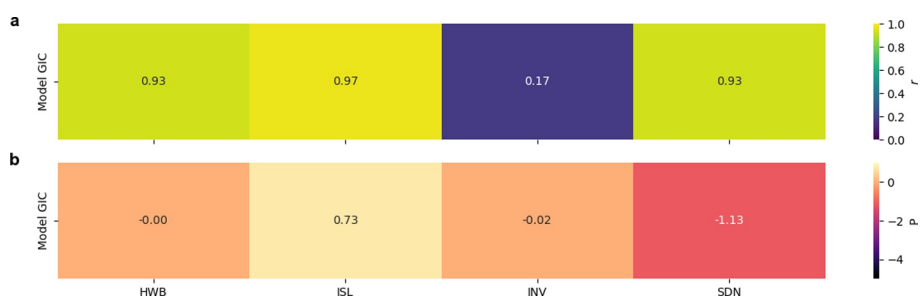

Figure 7. The linear Pearson correlation coefficient ("r," (a)) and Prediction Efficacy ("P," (b)) between the Geomagnetically Induced Current (GIC) recorded at four locations in New Zealand (HWB, ISL, INV and SDN) and the GIC modeled using the thin sheet technique using the magnetic field recorded at EYR.

of the South Island we see discrepancies begin to appear between the observations and the model results (i.e., Figures 6d, 6f, and 6g). While the predicted "shape" of the GIC is consistent close to Dunedin, with Pearson correlations of 0.93 (i.e., HWB and SDN, Figures 6d and 6g), the magnitudes of the GIC are not well reproduced, as demonstrated by the low prediction efficacy ($P \sim 0$ and -1, Figure 7b). Given the close geographical proximity of these transformers ($\sim$5 km), the difference in both model and observations highlights the importance of the network topology and properties in determining the GIC. Finally, at the southernmost location we see that the shape of the GIC is poorly reproduced (INV, Figure 6f), with an r of 0.17. The prediction efficacy is also low at $\sim$0, showing that the GIC is substantially underestimated. We attribute the discrepancy in these locations to uncertainty in the network topology at this time, though there may also be an impact of using the (more distant) EYR data as input.

5. Discussion

In this study we have shown the development of a mid-latitude ionospheric current system that has formed in the morning sector, giving rise to unexpectedly large and sustained GICs in the New Zealand power network. We now discuss these observations in the context of the driving processes, as well as the implications for mid-latitude locations, proxies of magnetospheric activity and GICs, and future GIC modeling efforts.

5.1. Morning Sector Impact: Physical Processes

Many geomagnetic phenomena are organized by local time, or only occur within specific regions (e.g., Rogers et al., 2021). Of relevance for this study, dawn local times have been highlighted by several studies as a "hot spot" for severe ground-level space weather. Schillings et al. (2022) highlight two local time sectors that see the largest spikes of dB/dt (i.e., H'): pre-midnight, and the morning sector. Schillings et al. (2022) and other recent studies (e.g., Hodnett et al., 2025) have related such morning sector activity to omega bands, though we note that other studies attribute such activity to phenomena such as auroral streamers (e.g., Zou et al., 2022), though both streamers and omega bands may share a common cause such as the evolution of flow bursts within the magnetotail (Forsyth et al., 2020; Henderson, 2022; Milan et al., 2024). However, these auroral phenomena have a different magnetic frequency content to the phenomena at the heart of this case study (i.e., typically Pc5 or Ps6, 150–600s or periods of a few 10s of minutes: Wild et al. (2000); Viljanen et al. (2001); Pulkkinen and Kataoka (2006)), and are typically observed at earlier MLTs (i.e., 02–03 MLT: Partamies et al. (2017); Apatenkov et al. (2020)). Nonetheless, such auroral phenomena may explain the higher latitude ($\sim$65°), more localized magnetic field signatures that peak during epochs γ and ϵ (i.e., Figures 4 and 5).

Another key dawn-sector phenomenon that has been linked to space weather impact is the possible diversion of the ring current into the ionosphere in the dawn region (Ohtani et al., 2018). Such an ionospheric current wedge would be closed with upward FACs on its western edge and downward FACs on the eastern. Ohtani (2021) posits that such a configuration could be driven by enhanced convection, which would be consistent with strong solar wind driving we see in this storm (Figures 1 and 3). The presence of such a dawnside current wedge has previously been diagnosed through the use of local time-limited indices (i.e., the SMR indices), where the discrepancy between dawn (SMR06) and dusk (SMR18) indicates an asymmetry (e.g., Bower et al., 2025). However, typically this asymmetry has the opposite sign to that observed here (i.e., $|\text{SMR06}| > |\text{SMR18}|$), where the smaller deflection of SMR at dawn is inferred to be symptomatic of the diversion into the ionosphere. In our case, SMR at dawn is depressed more due to the contamination of SMR with the mid-latitude ionospheric current. For the more typical scenario, such a diverted (and therefore ionospheric) current would be present at higher latitudes than are amalgamated by SMR (>50°).

Our primary hypothesis is that we are seeing the ionospheric manifestation of the diverted ring current, which forms a steadily increasing ionospheric current at mid-latitudes, a set-up driven by the very strong and steady convection electric field in this storm. However, it is curious that such an ionospheric diversion of the ring current is so "steady" at EYR, showing a slow progression. Most studies investigating the impact of such diagnose these intervals through their large, rapid changes of the ground magnetic field (e.g., Bower et al., 2024, 2025).

5.2. Mid-Latitude Impact

This case study represents a useful example showing how space weather can have notable impacts on mid-latitude locations, even for what does not seem to be an extreme geomagnetic storm. While the magnitude of the GICs in

New Zealand during this event are not extreme, Clilverd et al. (2025) found that at around 30 A of GIC measurable reactive power impact can be observed. Taking the limits described by Mac Manus, Rodger, Dalzell, et al. (2022), a level of 30 A could only be tolerated for 180 min (in a single phase transformer). In this case study the observed GICs were just short of that current, however it was sustained for far longer than would have been expected. We now consider two important hypothetical scenarios: the first where the magnetic field perturbation was larger, and the second where a different mid-latitude location (the UK) was exposed to the same ionospheric current system. This allows us to examine whether this phenomenon in the future may be at risk of causing thermal damage to power network infrastructure (i.e., Mac Manus, Rodger, Dalzell, et al., 2022), and whether other mid-latitude locations would be vulnerable, or if this problem would be restricted to New Zealand due to some quirk of geology or infrastructure.

5.2.1. Hypothetical Impact: Scaling

Using the modeling results in Figure 6, we may test simple hypothetical scenarios. Specifically, the input and output of the thin-sheet modeling may be scaled by the same linear relations. For example, if the size of the magnetic perturbation is doubled (i.e., the minimum B_N changes from −300 nT to −600 nT) then the modeled GIC will also double. Given we have shown the model performs excellently where the network configuration is well known, we can use this relation to estimate potential GIC for a hypothetical scenario.

For this type of event there are two clear ways in which the magnetic perturbation would be increased: (a) through an increase in the ionospheric current, and (b) through movement of the ionospheric current (c.f. Beggan, 2015). First, we have attributed this event to a diversion of the ring current into the ionosphere (Ohtani, 2021), and so it stands to reason that if the original ring current were stronger, or more of the current were diverted into the ionosphere then the impact would be greater. This type of event is poorly understood, and more work is needed, however we hypothesize that this may be the case if the driving (i.e., convection) were even stronger. Second, our New Zealand magnetic field data come from EYR, which is located at an absolute geomagnetic latitude of 50°. However, we have shown that MGD (at 54° in the Northern hemisphere) records a much larger B_N perturbation of ∼900 nT (Figure 4). Therefore, it is likely that the main impact of the ionospheric current is located at latitudes poleward of EYR. This may also change the orientation of the magnetic field change. A future, larger geomagnetic storm may involve such an ionospheric currents at lower latitudes, this would increase the impact at a location such as EYR.

With the considerations above, we test a tripling of the magnetic perturbation observed at EYR–this is effectively scaling the EYR observations to reach the maximum perturbation observed at MGB (five degrees higher in absolute latitude). We hypothesize that this would correspond to a larger storm, where the ring current is more intense, and perhaps the main impact is at a slightly lower latitude. At ISL we see the best model predictions (Figure 7), but the GIC measured here is small (∼4 A). Tripling the magnetic perturbation would not generate currents of the order suggested to be a problem by Mac Manus, Rodger, Dalzell, et al. (2022) (i.e., only ∼12 A). Lower down the South Island at HWB, the model over-predicts moderately, peaking at around 20 A, while the observations peak at 15 A. If we triple the observed GIC here, we drop below the −30 A "threshold" (Clilverd et al., 2025) for around 30 min, peaking at −59 A (near epoch δ). Mac Manus, Rodger, Dalzell, et al. (2022) state that this approximate level of GIC could be tolerated for over an hour (in a single phase transformer), but nevertheless this is a considerable threat from a previously understudied phenomenon.

5.2.2. Hypothetical Impact: United Kingdom

This event is notable in that its impact is at lower latitudes than would normally be expected for a G4 storm. In this regard, it is instructive to assess the potential impact in another location for which the necessary geological models are available: specifically we speculate as to how such a mid-latitude event might impact the UK. Further we test the second most common form of geoelectric field modeling commonly deployed: that based upon Magnetotelluric (MT) surveys. We note that this method has been used in New Zealand, and shown to perform similarly to thin-sheet modeling in this location for long-period disturbances (e.g., Pratscher et al., 2024). Unfortunately in the UK the transformer level network topology is not publicly available, and so we must limit our consideration to the modeled geoelectric field.

The UK is located at similar absolute geomagnetic latitude to New Zealand, and so we test a hypothetical event in which the UK observed the same magnetic field observations as were recorded at EYR (i.e., Figures 6a and 6b).

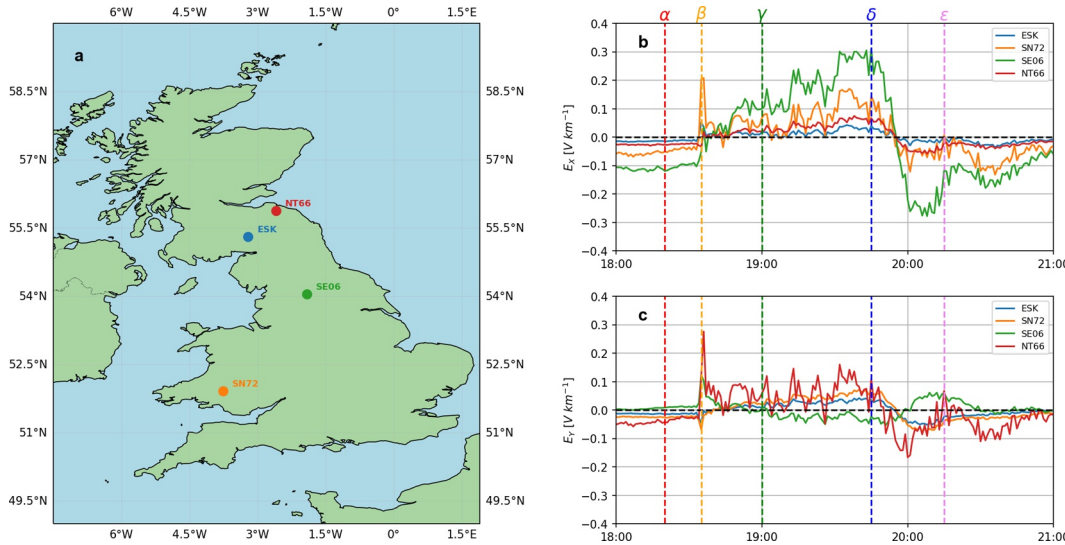

Figure 8. Modeling the ground impact in the United Kingdom with Magnetotelluric modeling. On the left (a), a map of the United Kingdom with the four locations (HT66, ESK, SE06 and SN72 marked). On the right, panels (b and c) show the modeled geoelectric field at the four locations across the UK, in the North and East directions respectively. As above, five epochs (α, β, γ, δ, and ϵ) are marked throughout the storm.

We utilize historical MT surveys of the UK, including a recent effort that expanded the number of sites to 70 (Hübert et al., 2025). Given the limited spatial coverage of the magnetic field data in New Zealand, we assume no spatial variation across the UK. One minute magnetic field data is used. Similar to other approaches (e.g., Campanyà et al., 2019; Malone-Leigh et al., 2023), we derive the time series of the geoelectric field using the impedance tensors at each site (in frequency space).

Figure 8 shows the results of this process at four test locations. Figure 8a shows a map of the UK on which the four locations are marked (HT66, ESK, SE06 and SN72). Figures 8b and 8c then show the modeled geoelectric field (E_X and E_Y respectively). These four locations have been selected to demonstrate a range of responses due to differences in their underlying geology. We can observe a range of electric field responses coincident with the SC at epoch β, which in some locations is followed by long interval, moderate geoelectric fields, peaking at around epoch δ.

The long-interval geoelectric fields are of most interest to this study, and at SE06 they build over time (as seen with the GIC in New Zealand), peaking at around 0.3 V km^{-1} at epoch δ. However, we can see a wide range of behavior across the four locations, with two locations (ESK, NT66) seeing little response in E_X (i.e., $<$0.1 V km^{-1}) at epoch δ. Meanwhile, NT66 shows stronger responses in E_Y, potentially linked to shorter period activity (i.e., the SC or H', Figure 2). The location where we see the largest electric fields (SE06, in E_X) is located close to an interesting geological feature noted by Montiel-Álvarez et al. (2025), where they modeled intense geoelectric fields during the October 2024 geomagnetic storm.

Importantly our modeling efforts have shown that while the impact of this event was observed in New Zealand, a similar event timed when the UK was at dawn may have an impact in some locations. While most of the UK would have seen relatively small geoelectric fields ($<$0.1 V km^{-1}), some locations would see peak geoelectric fields of $\sim$0.3 V km^{-1}. While these are more than an order of magnitude smaller than that modeled during the March 1989 storm, the levels are directly comparable to those modeled in England during the September 2017 storm (Hübert et al., 2025), and sustained for a longer period of time. For more recent context, the May 2024 geomagnetic storm was inferred to cause electric fields of the order of 1 V km^{-1} in the UK (Lawrence et al., 2025). We also note that railway operations would be unaffected, as signaling mis-operation is only observed for extreme peaks in activity, of the order several V km^{-1} (Patterson et al., 2023), rather than sustained, more moderate electric fields.

5.3. Implications for Geomagnetic Indices

In this case study, we have presented an example where the SYM-H index in particular has been shown to be contaminated by (likely rare) strong mid-latitude current systems. Likewise auroral indices (e.g., SML) have been shown to be impacted due to the latitudes considered within their construction.

5.3.1. Ring Current Indices

We have used several geomagnetic indices in this study, SYM-H and SMR in particular, designed to indicate the strength of the ring current. These indices are constructed through a combination of magnetometers, though the stations involved and their number vary between indices (e.g., Iyemori, 1990; Katus & Liemohn, 2013; Newell & Gjerloev, 2012). The more typical SYM-H index has fewer contributing stations, and a two-stage storm main phase can be seen (i.e., Figures 1 and 3). On closer inspection we showed that this first stage is due to a mid-latitude ionospheric current (Epochs β to δ), rather than a steadily increasing ring current. In contrast, SMR appears to average over these factors and returns a much smoother storm main phase (between epoch β and ϵ). This suggests that the larger number of stations that contribute to SMR act to remove the transient impact of longitudinally limited features, though they are inherently contributing to the overall index (e.g., the difference between the MLT-limited SMR indices in Figure 3).

These issues compound challenges facing studies that attempt to forecast such ring current indices (e.g., Collado-Villaverde et al., 2023; Siciliano et al., 2020), as well as the use of such indices in extreme storm analyses (e.g., Bergin et al., 2023; Ohtani, 2022). This is in addition to complications inherent in assuming symmetry of the ring current and the impact of FACs (Love & Mursula, 2024).

5.3.2. Auroral Indices

Geomagnetic substorms are a key type of magnetospheric activity, and one of the primary methods by which they are identified is through the use of auroral indices (i.e., AL or SML), for example, the SOPHIE method (Forsyth et al., 2015). Substorms are identified through strong negative excursions of the index, which are themselves based upon the B_X component of the magnetic field observed at various auroral magnetometer stations. In our case study, we highlighted that the SML index has remarkably little substorm-like structure in this interval (Figure 3) despite the strong driving of the magnetosphere (strong negative B_Z).

During this geomagnetic storm the SOPHIE method picks out two substorm-like events at 18:31 and 19:30. SML during both of these times is dominated by stations near dawn, which would be unusual for substorm-related currents (Frey & Mende, 2006; Lao et al., 2025; Walsh et al., 2014). As shown in Figure 5bi, the first identification may be related to the intensification of existing ionospheric current systems at the arrival of the interplanetary shock. The second event at 19:30 was detected at lower latitudes (54°), and likely represents the intensification of the mid-latitude current wedge (the core focus of this study). This case study represents a good example of the challenges of using global auroral indices to identify substorm-related activity, a topic of intense recent interest. Lao et al. (2025) outlined the challenges of separating convection-related intervals from substorms, suggesting that this may not be possible based solely upon the indices themselves. Meanwhile, Hodnett et al. (2025) highlighted that omega band activity (i.e., negative excursions of the north-south magnetic field) in the dawn region can be misidentified as substorms (Milan et al., 2024). These considerations likely contribute to why the association between substorm identification methods using different data sources show poor association (i.e., less than 50% coincidence) (Lao et al., 2024).

5.4. Evaluating Common Magnetic Proxy Measurements

Due to the limited availability of GIC data around the globe, and its specificity to a contemporaneous power network configuration (e.g., Mac Manus et al., 2023; Parry et al., 2025), many studies rely upon proxy quantities to indicate when significant GICs may arise. We now evaluate how two common proxy quantities capture the long-period activity outlined in this study.

5.4.1. H'

The most commonly used proxy for GICs is the rate of change of the geomagnetic field, calculated in a few different ways (Fielding et al., 2025). This is under the assumption that large rates of change of the geomagnetic

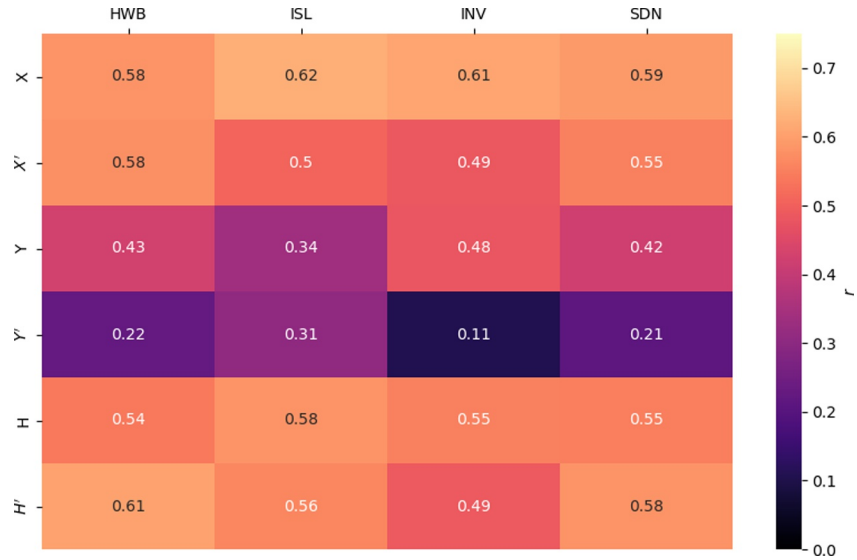

Figure 9. The linear Pearson correlation coefficient (r) between the Geomagnetically Induced Current recorded at four locations in New Zealand (HWB, ISL, INV and SDN) and the magnetic field (X, Y and H) and rate of change of the magnetic field (indicated with′ notation) recorded at EYR.

field are a necessary condition for large GICs (Viljanen et al., 2001). Indeed, in the few suitable long-duration data sets, the correlation between the rate of change of the horizontal magnetic field (e.g., H') and observed GIC is high ($r > 0.75$) (e.g., Mac Manus et al., 2017). Splitting out individual driving processes (A. W. Smith et al., 2022) and locations (Mac Manus et al., 2017; A. W. Smith et al., 2024) can dramatically improve this correlation. We note that even different types of the same process can lead to different correlations (A. W. Smith et al., 2025). However, studies have also shown good correlation with the horizontal ground magnetic field, and even individual vector components (e.g., B_X and B_Y) of the magnetic field, which will capture more longer-period (i.e., tens of minutes) changes, for example, those GICs related to Pc5 waves and similar phenomena (Heyns et al., 2021).

Figure 9 shows the linear (Pearson) correlation (r) obtained between the recorded GIC at the four locations in New Zealand (Figures 2 and 6) and several different facets of the ground magnetic field. We test the North, East and horizontal magnetic field, and their corresponding one-minute rates of change. Broadly, for this storm we see the poorest correlations with the B_Y component (denoted Y) and Y', and the best for X (B_X) and H (along with X' and H'). The poor correspondence of B_Y to the GIC is likely a reflection of the regional geology and the orientation of the power network. At three out of four locations (ISL, INV and SDN) we see the closest relationship between B_X and GIC, with H' being slightly better for HWB. The high performance of B_X was expected, given the morphology present in Figure 6. However, with so many different processes active during this storm (i.e., SC, ionospheric currents and ring current) it is no surprise that the overall r values are relatively low (maximum $r \sim 0.6$). We have also highlighted the importance of the network topology and properties in determining the resulting GIC, another factor that would challenge the use of H' as an accurate proxy measurement.

5.4.2. GIC Index-Like Proxy

While H' or equivalent proxies have been shown to well replicate both peak GICs (Rodger et al., 2017) and longer time series during storms (Mac Manus et al., 2017), they can only ever represent a narrow frequency range of magnetic perturbations (i.e., minute-to-minute changes), albeit one that is typical of GICs. An alternative proxy is the GIC index, which uses the plane wave approximation and is more accurately described as a proxy of the induced absolute geoelectric field (Marshall et al., 2010, 2011). GIC proxies constructed in such a fashion have been shown to have excellent correspondence to measured GICs (Waters & Marshall, 2026). Full details as to how our GIC index-like proxy has been calculated are reported in Appendix C, but we note here that we do not use any details of the geological conductivity in the construction of this proxy.

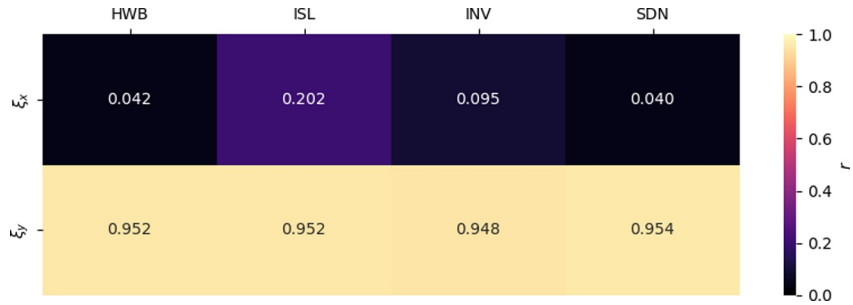

Figure 10. The linear Pearson correlation coefficient (r) between the Geomagnetically Induced Current (GIC) recorded at four locations in New Zealand (HWB, ISL, INV and SDN) and the X and Y components of the GIC Index (ξ_X, ξ_Y).

Figure 10a shows the correlation between our calculated GIC proxy in the X (ξ_X) and Y (ξ_Y) directions, and the GIC measured at the four locations of interest in this study. The first thing that stands out is the excellent ($r = 0.95$) linear correlations between ξ_Y and the GIC at all four locations (Figure 10), in three out of the four locations these exceed the correlations obtained by the full thin sheet modeling approach (Figure 7). This also suggests that such GIC index-like proxies may be well suited to evaluate cumulative long-term impacts (Zois, 2013). These results are similar to that obtained by Waters and Marshall (2026) in their study of the Australian power network. The excellent correlations are obtained by the ξ_Y index, and not the ξ_X index (which shows very poor correlations), demonstrates the link between the network configuration and resulting GIC.

5.5. Modeling Implications

As described above, the correspondence between the various simple magnetic proxies (B_X, B_Y, H, and their respective one-minute rates of change) and the GIC observed at each of the four locations is weak at best ($r < 0.7$). This is likely due to the plethora of different magnetospheric phenomena active during the interval, and the dominance of an unusual long-interval GIC for which these proxies are not ideal. A proxy with more thorough frequency consideration was shown to be much better (e.g., Figure 10; Waters and Marshall (2026)). In Figure 6 we then showed the capability of a typical thin sheet modeling method to calculate the GIC from the magnetic field data itself. At three of the four locations (HWB, ISL and SDN) the linear correlation between the GIC model and observations are 0.93, 0.97 and 0.93 respectively. The exception to this is at INV, where we discussed how uncertainties with the network configuration at the Southern end of the network precluded accurate modeling. This highlights how close collaboration is required between academia and industrial partners. However, we have shown that typical thin-sheet modeling can capture this form of GIC hazard.

We have also tested a hypothetical scenario where the UK was subject to the same magnetic conditions as EYR in the interval. The MT modeling in this region showed that it does reproduce such long-interval geoelectric fields and that they are very dependent upon the geology of the location, with most locations seeing only very small geoelectric fields. In this regard, we have shown both common methods of estimating the geoelectric field (and GIC, subject to power network model availability) are capable of reproducing this hazard, and our results highlight the importance of knowing the details of the power network (e.g., topology and resistances) (Blake et al., 2018; Mac Manus, Rodger, Ingham, et al., 2022; Parry et al., 2025).

5.6. Future Research Considerations

This event represents an unusual observation: a slow but consistently building current wedge in the mid-latitude ionosphere. In future, work should be undertaken to isolate the conditions under which such a current wedge is likely to form. It is of paramount importance to determine the controlling factors for the latitude and strength of the ionospheric current (e.g., Section 5.2.1), as these directly determine the potential impact. More examples will be needed, and we suggest that the strong and persistent solar wind convection electric field may be one of the key drivers of such an event.

This work has also highlighted the need to include and understand the configuration of the power network. More work should be undertaken in collaboration with industrial stakeholders to ensure that this critical step in the chain of GIC modeling is accounted for.

6. Conclusions and Summary

In this study we have detailed novel observations of GICs made in New Zealand during a G4 storm in 2015, and examined their likely cause. During the geomagnetic storm in June 2015, we observed a ramp-like increase in GIC as measured at four locations across the South Island of New Zealand. This GIC, though not large by itself, increased for a period of ∼70 minutes, to a level exceeding that during the preceding interplanetary shock impact (at 3 out of 4 locations). This storm showed a notably intense convection electric field, due to high solar wind velocity ($\sim 700\,\mathrm{kms}^{-1}$) and strongly negative B_Z^{GSM} ($\sim -40\,\mathrm{nT}$).

The ramp-like GIC increase was inferred to be a result of large-scale, mid-latitude (∼55° MLat) ionospheric current wedge localized in the dawn sector. This ionospheric current wedge was confirmed through the presence of corresponding mid-latitude FACs. It is possible that this was caused by a diversion of the ring current into the ionosphere, as a result of the high convection electric field (e.g., Ohtani, 2021).

Given the unusual nature of this ground-level space weather hazard, we show that the most common magnetic field proxy (H') shows only limited ability to describe the resulting GIC ($r < 0.7$), while a more complex GIC Index-like proxy (Marshall et al., 2011) is much more capable of capturing the relevant behavior ($r \sim 0.95$). This highlights that the use of simple GIC proxies (i.e., H') should be made with care, and that they should be "calibrated" for the type of geomagnetic activity. Nonetheless, we confirmed that present GIC modeling methods (i.e., thin-sheet models) are capable of capturing the impact ($r \sim 0.95$), when requisite power network information is available. We highlight the importance of knowing the local network topology and properties, showing how two geographically close locations (∼5 km) record distinctly different current magnitudes. Close collaboration is needed between academia and industrial partners.

We tested two hypothetical scenarios: the first where the ground geomagnetic perturbation is larger in New Zealand–matching that observed at a slightly higher latitude. The scaling is linear between the input perturbation and GIC, and we infer that reactive power impact (i.e., GIC > 30 A) would be observed for around 30 min at a sensitive location (HWB). For the second scenario we model the results if the UK, at a similar geomagnetic latitude, were to experience such ionospheric conditions to test if New Zealand is uniquely vulnerable. We find that the resulting hypothetical geoelectric fields can be relatively large $\left(\sim 0.3\,\mathrm{V\,km}^{-1}\right)$, of the order of those modeled during the September 2017 storm, and sustained for a longer interval. However, we also find that most locations see very small geoelectric fields as a result of their local subsurface conductivity. This phenomenon is therefore not limited to New Zealand and should be accounted for at other mid-latitude locations.

In the course of investigating the storm, we show how such mid-latitude ionospheric currents can contaminate both ring current indices (i.e., SYM-H) and auroral indices (i.e., SML), and we discuss the implications for extreme event studies and present forecasting efforts.

Appendix A: Broader Storm Interval

In this case study we have focused exclusively on a period of time between 17 : 30 and 22 : 00 UT on the 22 June 2015, however this storm occurred within a series of complex solar wind structures (Gopalswamy et al., 2018). Figure A1 shows a time series of the solar wind properties (and SMR) during a 6 day window around the main case study.

We see that prior to the main CME arrival (epoch β: 18:35 UT on the 22nd June), there are two smaller shocks at approximately 17:00 on the 21st and 06:00 UT on the 22nd June, most clearly visible as jumps/rapid changes in the solar wind density and ion and electron spectrograms (Figures A1d–A1f). These two interplanetary shocks are not as large as the one considered in the main interval, in either magnetic field strength (maximum —B—

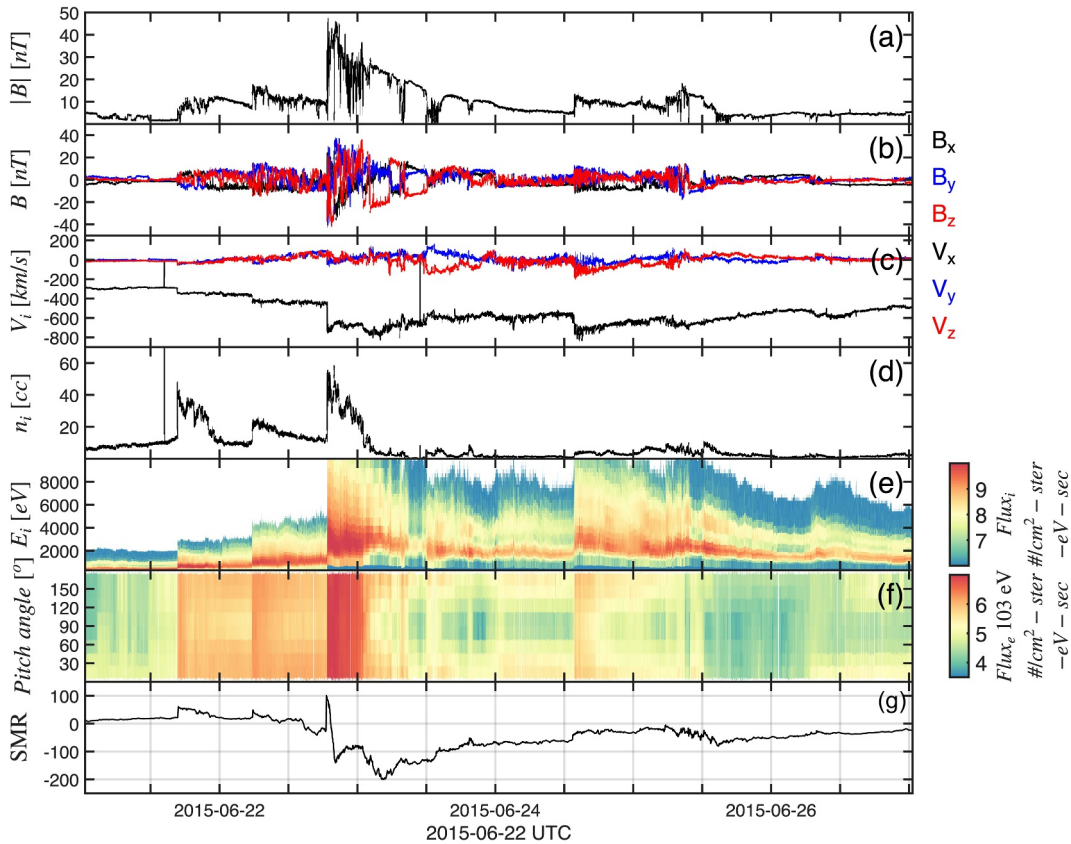

Figure A1. A 6 day overview of the storm interval from the perspective of the WIND spacecraft upstream of the Earth. The WIND observations have been time shifted such that the arrival of the main interplanetary shock within the study (interval β) is aligned with the shock arrival in SMR (18:35 UT, 22 June). The panels describe the total magnetic field strength (a), three components of the interplanetary magnetic field (b), three components of the solar wind velocity (c), solar wind density (d), ion spectrogram (e), electron pitch angle spectrum (f) and SMR index (g).

$\sim$10−20 nT) or velocity (maximum $V_X \sim 400$ km s^{-1}), but nevertheless may have preconditioned the magnetospheric system.

Second, the end of the case study is just before midnight on the 22nd June, during what appears (from SMR or SYM-H, Figure 3) to be the storm recovery phase: steadily increasing SMR back toward zero. However, later within the CME's magnetic cloud we see complex structure and two periods of intense and sustained negative B_Z (Figure A1b). Correspondingly, early on the 23rd June the SMR index decreases once more to $\sim$−200 nT, signifying a further intensification of the ring current. However, this is beyond the scope of the current case study–the unusual mid-latitude current system is not present at this later time.

Appendix B: AMPERE Inter-Hemispheric Comparison

Within Figure 5 we compared the ground-based magnetometer observations with the FACs as inferred from AMPERE, both within the Northern hemisphere. Figure B1 displays the same intervals as Figure 5, but with an additional column (iv) on the right including AMPERE data from the Southern hemisphere. For the purposes of this case study, the Northern and Southern hemisphere AMPERE are qualitatively equivalent, with the FACs strengthening at mid-latitudes, peaking at epoch δ. We note that some studies have noted that the Southern hemispheric currents are underestimated in pre-2017 data (Hatch et al., 2022). We do see differences in the current strength, with the Southern hemisphere current being noticeably weaker in epochs α and β. However, we mainly interpret this as a seasonal effect–the storm occurs during Northern hemisphere summer, when the ionospheric conductance is weaker in the Southern hemisphere.

10.1029/2026SW005032

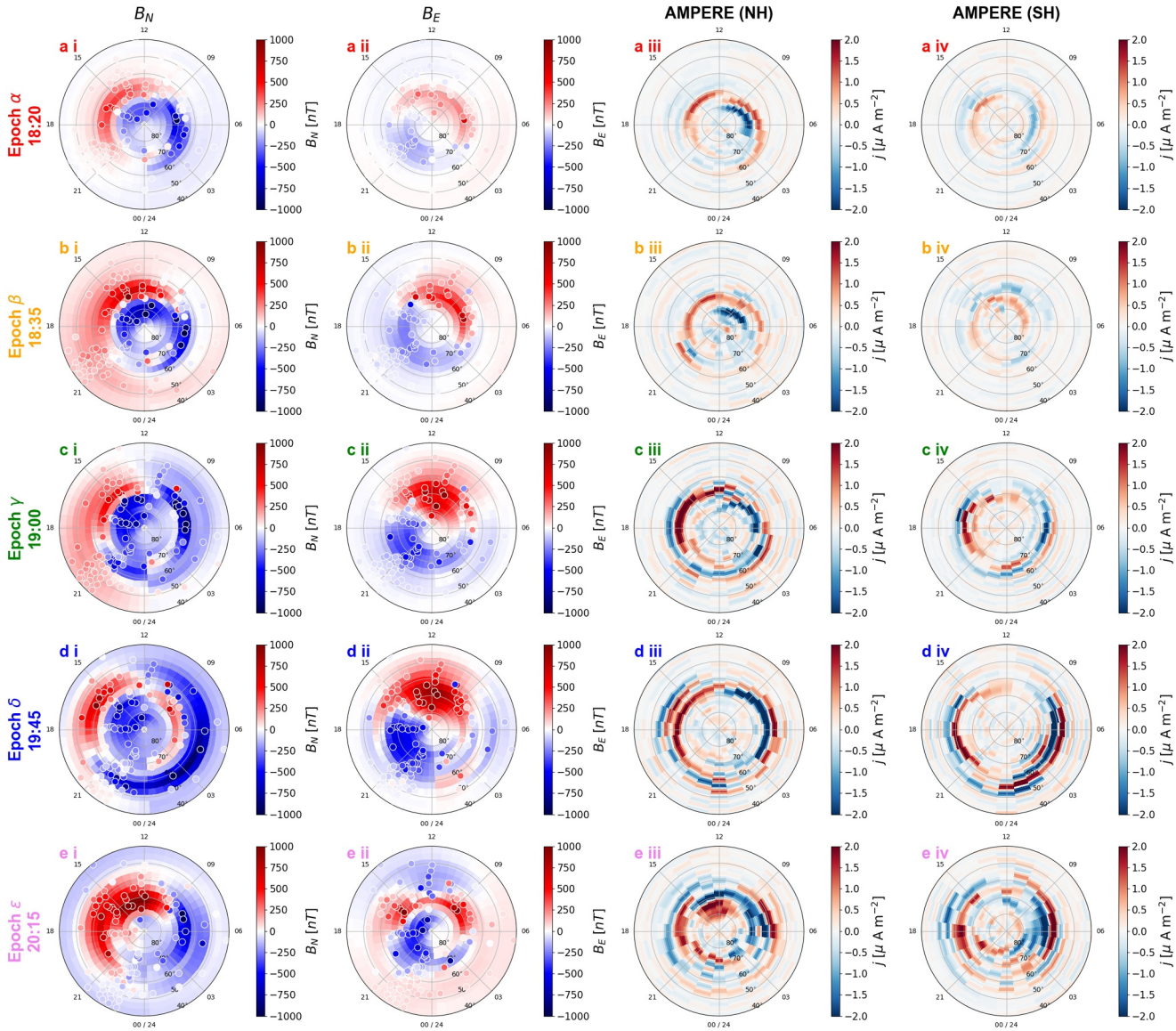

Figure B1. Geomagnetic polar plots displaying SuperMAG observations of the Northern hemisphere geomagnetic field (left: i and ii) and Active Magnetosphere and Planetary Electrodynamics Response Experiment (AMPERE) observations of the field aligned currents (right: iii, iv) during the five key periods highlighted throughout the storm. The format is as in Figure 5, with the addition of the Southern hemisphere AMPERE data (panels iv).

Appendix C: GIC Proxy Calculation

To calculate our GIC proxy, we use a similar method to Marshall et al. (2011), using one-minute resolution data from the EYR magnetometer ($B_X(t)$ and $B_Y(t)$). First, the Fourier transform of the magnetic field is taken, giving $B_X(f)$ and $B_Y(f)$. The GIC proxies for the X and Y directions are then calculated as:

$$\xi_X = \mathrm{FFT}\{B_Y(f)Z(f)\}^{-1} \tag{C1}$$

$$\xi_Y = \mathrm{FFT}\{B_X(f)Z(f)\}^{-1} \tag{C2}$$

Acknowledgments
For the ground magnetometer data we gratefully acknowledge: INTERMAGNET, Alan Thomson; CARISMA, PI Ian Mann; CANMOS, Geomagnetism Unit of the Geological Survey of Canada; The S-RAMP Database, PI K. Yumoto and Dr. K. Shiokawa; The SPIDR database; AARI, PI Oleg Troshichev; The MACCS program, PI M. Engebretson; GIMA; MEASURE, UCLA IGPP and Florida Institute of Technology; SAMBA, PI Eftyhia Zesta; 210 Chain, PI K. Yumoto; SAMNET, PI Farideh Honary; IMAGE, PI Liisa Juusola; Finnish Meteorological Institute, PI Liisa Juusola; Sodankylä Geophysical Observatory, PI Tero Raita; UiT the Arctic University of Norway, Tromsø Geophysical Observatory, PI Magnar G. Johnsen; GFZ German Research Centre For Geosciences, PI Jürgen Matzka; Institute of Geophysics, Polish Academy of Sciences, PI Anne Neska and Jan Reda; Polar Geophysical Institute, PI Alexander Yahnin and Yarolav Sakharov; Geological Survey of Sweden, PI Gerhard Schwarz; Swedish Institute of Space Physics, PI Masatoshi Yamauchi; AUTUMN, PI Martin Connors; DTU Space, Thom Edwards and PI Anna Willer; South Pole and McMurdo Magnetometer, PI's Louis J. Lanzarotti and Alan T. Weatherwax; ICESTAR; RAPIDMAG; British Artarctic Survey; McMac, PI Dr. Peter Chi; BGS, PI Dr. Susan Macmillan; Pushkov Institute of Terrestrial Magnetism, Ionosphere and Radio Wave Propagation (IZMIRAN); MFGI, PI B. Heilig; University of L'Aquila, PI M. Vellante; BCMT, V. Lesur and A. Chambodut; Data obtained in cooperation with Geoscience Australia, PI Andrew Lewis; PENGUIn, co-PIs Bob Clauer, Michael Hartinger, and Zhonghua Xu; MagStar, PI Jennifer Gannon; LISN PI Cesar Valladares; Geophysical and Astronomical Observatory of the University of Coimbra, PI Paulo Ribeiro; Leibniz Institute of Atmospheric Physics, PI Jorge Chau; SuperMAG, PI Jesper W. Gjerloev; Data obtained in cooperation with the Australian Bureau of Meteorology, PI Richard Marshall. The authors thank the New Zealand Institute for Earth Science Limited (Earth Sciences New Zealand), formerly known as GNS Science, for supporting its operation and INTERMAGNET for promoting high standards of magnetic observatory practice (www. intermagnet.org). AWS would like to thank J. A. Wild, N. Colville and A. Grocott for useful discussions. AWS was supported by NERC Independent Research Fellowship NE/W009129/1. JCC was supported by Science and Technology Facilities Council (STFC) Ernest Rutherford Fellowship ST/V004883/1. MTW was supported by the Science and Technology Facilities Council (STFC) Ernest Rutherford Fellowship (ST/X003663/1). The UK magnetotelluric data were collected under the NERC SWIMMR N4 programme NE/V002694/1.

where $\mathrm{FFT}\{\}^{-1}$ represents the inverse Fourier transform, and $Z(f)$ is our chosen frequency domain filter given by:

$$Z(f) = \sqrt{\frac{f}{f_N}} e^{i\frac{\pi}{4}} \tag{C3}$$

with f_N representing the Nyquist frequency.

Conflict of Interest

The authors declare no conflicts of interest relevant to this study.

Availability Statement

The results presented in this paper rely on the data collected at the Eyrewell magnetometer station. These data can be found on INTERMAGNET or (GNS Science, 2022). We acknowledge use of NASA/GSFC's Space Physics Data Facility's CDAWeb service (at http://cdaweb.gsfc.nasa.gov) and OMNI data (Papitashvili & King, 2020). The Iridium-derived AMPERE data used in this paper can be obtained from the AMPERE Science Center (at https://ampere.jhuapl.edu/). The New Zealand electrical transmission network DC measurements were provided to us by Transpower New Zealand with caveats and restrictions. This includes requirements of permission before all publications and presentations and no ability to provide the observations themselves. Requests for access to these characteristics and the DC measurements need to be made to Transpower New Zealand. At this time, the contact point is M. Dalzell (Michael.Dalzell@transpower. co.nz). The analysis in this paper was performed using python, including the pandas (McKinney, 2010), NumPy (Van Der Walt et al., 2011), SciPy (Virtanen et al., 2020), emcee (Foreman-Mackey et al., 2012), and Matplotlib (Hunter, 2007) libraries.

References

Anderson, B. J., Angappan, R., Barik, A., Vines, S. K., Stanley, S., Bernasconi, P. N., et al. (2021). Iridium communications satellite constellation data for study of Earth's magnetic field. *Geochemistry, Geophysics, Geosystems*, *22*(8), e2020GC009515. https://doi.org/10.1029/2020GC009515

Anderson, B. J., Takahashi, K., & Toth, B. A. (2000). Sensing global Birkeland currents with iridium® engineering magnetometer data. *Geophysical Research Letters*, *27*(24), 4045–4048. https://doi.org/10.1029/2000GL000094

Apatenkov, S. V., Pilipenko, V. A., Gordeev, E. I., Viljanen, A., Juusola, L., Belakhovsky, V. B., et al. (2020). Auroral Omega bands are a significant cause of large geomagnetically induced currents. *Geophysical Research Letters*, *47*(6), e2019GL086677. https://doi.org/10.1029/2019GL086677

Beggan, C. D. (2015). Sensitivity of geomagnetically induced currents to varying auroral electrojet and conductivity models. *Earth Planets and Space*, *67*(1), 24. https://doi.org/10.1186/s40623-014-0168-9

Beggan, C. D., Beamish, D., Richards, A., Kelly, G. S., & Alan, A. W. (2013). Prediction of extreme geomagnetically induced currents in the UK high-voltage network. *Space Weather*, *11*(7), 407–419. https://doi.org/10.1002/swe.20065

Beland, J., & Small, K. (2004). Space weather effects on power transmission systems: The cases of Hydro-Quebec and transpower NewZealand Ltd [Proceedings Paper]. In I. Daglis (Ed.), *Effects of space weather on technology infrastructure* (Vol. 176, pp. 287–299). Springer.

Bergin, A., Chapman, S. C., Watkins, N. W., Moloney, N. R., & Gjerloev, J. W. (2023). Extreme event statistics in Dst, SYM-H, and SMR geomagnetic indices. *Space Weather*, *21*(3), e2022SW003304. https://doi.org/10.1029/2022SW003304

Blake, S. P., Gallagher, P. T., Campanyà, J., Hogg, C., Beggan, C. D., Thomson, A. W., et al. (2018). A detailed model of the Irish high voltage power network for simulating GICs. *Space Weather*, *16*(11), 1770–1783. https://doi.org/10.1029/2018SW001926

Bolduc, L. (2002). GIC observations and studies in the hydro-Québec power system. *Journal of Atmospheric and Solar-Terrestrial Physics*, *64*(16), 1793–1802. https://doi.org/10.1016/S1364-6826(02)00128-1

Bolduc, L., Langlois, P., Boteler, D., & Pirjola, R. (1998). A study of geoelectromagnetic disturbances in Québec, 1. General results. *IEEE Transactions on Power Delivery*, *13*(4), 1251–1256. https://doi.org/10.1109/61.714492

Boteler, D. H. (2003). Geomagnetic hazards to conducting networks. *Natural Hazards*, *28*(2–3), 537–561. https://doi.org/10.1023/a:1022902713136

Boteler, D. H. (2019). A 21st century view of the March 1989 magnetic storm. *Space Weather*, *17*(10), 1427–1441. https://doi.org/10.1029/2019SW002278

Boteler, D. H., & Pirjola, R. J. (2014). Comparison of methods for modelling geomagnetically induced currents. *Annales Geophysicae*, *32*(9), 1177–1187. https://doi.org/10.5194/ANGEO-32-1177-2014

Bower, G. E., Imber, S., Milan, S. E., Schillings, A., Fleetham, A. L., & Gjerloev, J. W. (2024). Location of geomagnetic disturbances in relation to the field aligned current boundary. *Journal of Geophysical Research: Space Physics*, *129*(10), e2024JA033039. https://doi.org/10.1029/2024JA033039

Bower, G. E., Milan, S. E., Imber, S., Schillings, A., Fleetham, A., Beggan, C., & Gjerloev, J. W. (2025). Asymmetry in the ring current during geomagnetic disturbances. *Journal of Geophysical Research: Space Physics*, *130*(3), e2024JA033492. https://doi.org/10.1029/2024JA033492

Campanyà, J., Gallagher, P. T., Blake, S. P., Gibbs, M., Jackson, D., Beggan, C. D., et al. (2019). Modeling geoelectric fields in Ireland and the UK for space weather applications. *Space Weather*, *17*(2), 216–237. https://doi.org/10.1029/2018SW001999

Camporeale, E., Cash, M. D., Singer, H. J., Balch, C. C., Huang, Z., & Toth, G. (2020). A gray-box model for a probabilistic estimate of regional ground magnetic perturbations: Enhancing the NOAA operational geospace model with machine learning. *Journal of Geophysical Research: Space Physics*, *125*(11), e2019JA027684. https://doi.org/10.1029/2019JA027684

This research was supported by the New Zealand Ministry of Business, Innovation & Employment Endeavour Fund Research Programme Contracts UOOX2002 and UOO2505.

Clilverd, M. A., Rodger, C. J., Brundell, J. B., Dalzell, M., Martin, I., Mac Manus, D. H., & Thomson, N. R. (2020). Geomagnetically induced currents and harmonic distortion: High time resolution case studies. *Space Weather*, *18*(10), e2020SW002594. https://doi.org/10.1029/2020SW002594

Clilverd, M. A., Rodger, C. J., Brundell, J. B., Dalzell, M., Martin, I., Mac Manus, D. H., et al. (2018). Long-lasting geomagnetically induced currents and harmonic distortion observed in New Zealand during the 7–8 September 2017 disturbed period. *Space Weather*, *16*(6), 704–717. https://doi.org/10.1029/2018SW001822

Clilverd, M. A., Rodger, C. J., Manus, D. H. M., Brundell, J. B., Dalzell, M., Renton, A., et al. (2025). Geomagnetically induced currents, transformer harmonics, and reactive power impacts of the Gannon storm in May 2024. *Space Weather*, *23*(4), e2024SW004235. https://doi.org/10.1029/2024SW004235

Collado-Villaverde, A., Muñoz, P., & Cid, C. (2023). Neural networks for operational SYM-H forecasting using attention and SWICS plasma features. *Space Weather*, *21*(8), e2023SW003485. https://doi.org/10.1029/2023SW003485

Coughlan, M., Keesee, A., Pinto, V., Mukundan, R., Marchezi, J. P., Johnson, J., et al. (2023). Probabilistic forecasting of ground magnetic perturbation spikes at mid-latitude stations. *Space Weather*, *21*(6), e2023SW003446. https://doi.org/10.1029/2023SW003446

Coxon, J. C., Milan, S. E., Carter, J. A., Clausen, L. B., Anderson, B. J., & Korth, H. (2016). Seasonal and diurnal variations in AMPERE observations of the Birkeland currents compared to modeled results. *Journal of Geophysical Research A: Space Physics*, *121*(5), 4027–4040. https://doi.org/10.1002/2015JA022050

Crack, M., Rodger, C. J., Clilverd, M. A., Mac Manus, D. H., Martin, I., Dalzell, M., et al. (2024). Even-order harmonic distortion observations during multiple geomagnetic disturbances: Investigation from New Zealand. *Space Weather*, *22*(5), e2024SW003879. https://doi.org/10.1029/2024SW003879

Dimmock, A. P., Lanabere, V., Johlander, A., Rosenqvist, L., Yordanova, E., Buchert, S., et al. (2024). Investigating the trip of a transformer in Sweden during the 24 April 2023 storm. *Space Weather*, *22*(11), e2024SW003948. https://doi.org/10.1029/2024SW003948

Dimmock, A. P., Rosenqvist, L., Hall, J. O., Viljanen, A., Yordanova, E., Honkonen, I., et al. (2019). The GIC and geomagnetic response over Fennoscandia to the 7–8 September 2017 geomagnetic storm. *Space Weather*, *17*(7), 989–1010. https://doi.org/10.1029/2018SW002132

Dimmock, A. P., Rosenqvist, L., Welling, D. T., Viljanen, A., Honkonen, I., Boynton, R. J., & Yordanova, E. (2020). On the regional variability of dB/dt and its significance to GIC. *Space Weather*, *18*(8), e2020SW002497. https://doi.org/10.1029/2020SW002497

Divett, T., Mac Manus, D. H., Richardson, G. S., Beggan, C. D., Rodger, C. J., Ingham, M., et al. (2020). Geomagnetically induced current model validation from New Zealand's South Island. *Space Weather*, *18*(8), e2020SW002494. https://doi.org/10.1029/2020SW002494

Divett, T., Richardson, G. S., Beggan, C. D., Rodger, C. J., Boteler, D. H., Ingham, M., et al. (2018). Transformer-level modeling of geomagnetically induced currents in New Zealand's South Island. *Space Weather*, *16*(6), 718–735. https://doi.org/10.1029/2018SW001814

Eastwood, J. P., Hapgood, M. A., Biffis, E., Benedetti, D., Bisi, M. M., Green, L., et al. (2018). Quantifying the economic value of space weather forecasting for power grids: An exploratory study. *Space Weather*, *16*(12), 2052–2067. https://doi.org/10.1029/2018SW002003

Fielding, S. A., Livermore, P. W., Beggan, C. D., Whaler, K. A., & Richardson, G. S. (2025). A comparison of methods to compute the rate of horizontal geomagnetic field variation. *Annales Geophysicae*, *43*(2), 687–700. https://doi.org/10.5194/angeo-43-687-2025

Fogg, A. R., Jackman, C. M., Malone-Leigh, J., Gallagher, P. T., Smith, A. W., Lester, M., et al. (2023). Extreme value analysis of ground magnetometer observations at Valentia observatory, Ireland. *Space Weather*, *21*(7), e2023SW003565. https://doi.org/10.1029/2023SW003565

Foreman-Mackey, D., Hogg, D. W., Lang, D., & Goodman, J. (2012). Emcee: The MCMC hammer. *Publications of the Astronomical Society of the Pacific*, *125*(925), 306–312. https://doi.org/10.1086/670067

Forsyth, C., Rae, I. J., Coxon, J. C., Freeman, M. P., Jackman, C. M., Gjerloev, J., & Fazakerley, A. N. (2015). A new technique for determining substorm onsets and phases from indices of the electrojet (SOPHIE). *Journal of Geophysical Research: Space Physics*, *120*(12), 10592–10606. https://doi.org/10.1002/2015JA021343

Forsyth, C., Sergeev, V. A., Henderson, M. G., Nishimura, Y., & Gallardo-Lacourt, B. (2020). Physical processes of meso-scale, dynamic auroral forms. *Space Science Reviews*, *216*(4), 46. https://doi.org/10.1007/s11214-020-00665-y

Freeman, M. P., Forsyth, C., & Rae, I. J. (2019). The influence of substorms on extreme rates of change of the surface horizontal magnetic field in the UK. *Space Weather*, *17*(6), 827–844. https://doi.org/10.1029/2018SW002148

Frey, H. U., & Mende, S. B. (2006). Substorm onsets as observed by IMAGE-FUV. Retrieved from http://www.ics8.ca/proc_files/frey.pdf

Gjerloev, J. W. (2012). The SuperMAG data processing technique. *Journal of Geophysical Research*, *117*(A9). https://doi.org/10.1029/2012JA017683

GNS Science. (2022). Preliminary 1-second and 1-minute data from Eyrewell (EYR) [Dataset]. https://doi.org/10.21420/APJY-5050

Gopalswamy, N., Mäkelä, P., Akiyama, S., Yashiro, S., Xie, H., & Thakur, N. (2018). Sun-to-earth propagation of the 2015 June 21 coronal mass ejection revealed by optical, EUV, and radio observations. *Journal of Atmospheric and Solar-Terrestrial Physics*, *179*, 225–238. https://doi.org/10.1016/J.JASTP.2018.07.013

Guillon, S., Toner, P., Gibson, L., & Boteler, D. (2016). A colorful blackout: The havoc caused by auroral electrojet generated magnetic field variations in 1989. *IEEE Power and Energy Magazine*, *14*(6), 59–71. https://doi.org/10.1109/MPE.2016.2591760

Hatch, S. M., Laundal, K. M., & Reistad, J. P. (2022). Testing the mirror symmetry of Birkeland and ionospheric currents with respect to magnetic latitude, dipole tilt angle, and IMF By. *Frontiers in Astronomy and Space Sciences*, *9*, 958977. https://doi.org/10.3389/FSPAS.2022.958977/TEXT

Henderson, M. G. (2022). Association of mesoscale auroral structures and breakups with energetic particle injections at geosynchronous orbit. *Frontiers in Astronomy and Space Sciences*, *9*, 742246. https://doi.org/10.3389/fspas.2022.742246

Heyns, M. J., Lotz, S. I., & Gaunt, C. T. (2021). Geomagnetic pulsations driving geomagnetically induced currents. *Space Weather*, *19*(2), e2020SW002557. https://doi.org/10.1029/2020SW002557

Hodnett, R. M., Milan, S. E., Nozawa, S., Raita, T., Gjerloev, J. W., Vines, S. K., & Paxton, L. J. (2025). Omega bands as a source of large dB/dt in the dawn sector. *Journal of Geophysical Research: Space Physics*, *130*(11), e2025JA034342. https://doi.org/10.1029/2025JA034342

Hübert, J., Eaton, E., Beggan, C. D., Montiel-Álvarez, A. M., Kiyan, D., & Hogg, C. (2025). Developing a new ground electric field model for geomagnetically induced currents in Britain based on long-period magnetotelluric data. *Space Weather*, *23*(8), e2025SW004427. https://doi.org/10.1029/2025SW004427

Hunter, J. D. (2007). Matplotlib: A 2D graphics environment [Software]. *Computing in Science & Engineering*, *9*(3), 90–95. https://doi.org/10.1109/MCSE.2007.55

Iong, D., McAnear, M., Qu, Y., Zou, S., Toth, G., & Chen, Y. (2024). Sparse variational contaminated noise Gaussian process regression with applications in geomagnetic perturbations forecasting. *Data Science in Science*, *3*(1), 2383281. https://doi.org/10.1080/26941899.2024.2383281

Iyemori, T. (1990). Storm-time magnetospheric currents inferred from mid-latitude geomagnetic field variations. *Journal of Geomagnetism and Geoelectricity*, *42*(11), 1249–1265. https://doi.org/10.5636/jgg.42.1249

Kappenman, J. G. (2018). Geomagnetic disturbances and impacts upon power system operation. *Electric Power Generation, Transmission, and Distribution: The Electric Power Engineering Handbook*, 17–1. https://doi.org/10.1201/9781315222424-17

Kärhä, O., Tanskanen, E. I., & Vanhamäki, H. (2023). Large regional variability in geomagnetic storm effects in the auroral zone. *Scientific Reports*, *13*(1), 1–6. https://doi.org/10.1038/s41598-023-46352-0

Katus, R. M., & Liemohn, M. W. (2013). Similarities and differences in low to middle latitude geomagnetic indices. *Journal of Geophysical Research: Space Physics*, *118*(8), 5149–5156. https://doi.org/10.1002/JGRA.50501

Keesee, A. M., Pinto, V., Coughlan, M., Lennox, C., Mahmud, M. S., & Connor, H. K. (2020). Comparison of deep learning techniques to model connections between solar wind and ground magnetic perturbations. *Frontiers in Astronomy and Space Sciences*, *7*, 72. https://doi.org/10.3389/fspas.2020.550874

Lao, C. J., Forsyth, C., Freeman, M. P., & Gjerloev, J. W. (2025). Separating DP1 and DP2 current pattern contributions to substorm-like intensifications in SML. *Journal of Geophysical Research: Space Physics*, *130*(4), e2024JA033592. https://doi.org/10.1029/2024JA033592

Lao, C. J., Forsyth, C., Freeman, M. P., Smith, A. W., & Mooney, M. K. (2024). On the association of substorm identification methods. *Journal of Geophysical Research: Space Physics*, *129*(9), e2024JA032762. https://doi.org/10.1029/2024JA032762

Lawrence, E., Beggan, C. D., Richardson, G. S., Reay, S., Thompson, V., Clarke, E., et al. (2025). The geomagnetic and geoelectric response to the May 2024 geomagnetic storm in the United Kingdom. *Frontiers in Astronomy and Space Sciences*, *12*, 1550923. https://doi.org/10.3389/fspas.2025.1550923

Lehtinen, M., & Pirjola, R. (1985). Currents produced in Earth condutor networks by geomagnetically-induced electric fields. *Annales Geophysicae*, *3*(4), 479–484. Retrieved from https://ci.nii.ac.jp/naid/10024499668/

Liu, L., Ge, X., Zong, W., Zhou, Y., & Liu, M. (2016). Analysis of the monitoring data of geomagnetic storm interference in the electrification system of a high-speed railway. *Space Weather*, *14*(10), 754–763. https://doi.org/10.1002/2016SW001411

Love, J. J., & Mursula, K. (2024). Challenging ring-current models of the Carrington storm. *Journal of Geophysical Research: Space Physics*, *129*(9), e2024JA032541. https://doi.org/10.1029/2024JA032541

Macho, E. P., Correia, E., Paulo, C. M., Angulo, L., & Vieira, J. A. G. (2020). Ionospheric response to the June 2015 geomagnetic storm in the South American region. *Advances in Space Research*, *65*(9), 2172–2183. https://doi.org/10.1016/J.ASR.2020.02.025

Mac Manus, D. H., Rodger, C. J., Dalzell, M., Renton, A., Richardson, G. S., Petersen, T., & Clilverd, M. A. (2022). Geomagnetically induced current modeling in New Zealand: Extreme storm analysis using multiple disturbance scenarios and industry provided hazard magnitudes. *Space Weather*, *20*(12), e2022SW003320. https://doi.org/10.1029/2022SW003320

Mac Manus, D. H., Rodger, C. J., Dalzell, M., Thomson, A. W., Clilverd, M. A., Petersen, T., et al. (2017). Long-term geomagnetically induced current observations in New Zealand: Earth return corrections and geomagnetic field driver. *Space Weather*, *15*(8), 1020–1038. https://doi.org/10.1002/2017SW001635

Mac Manus, D. H., Rodger, C. J., Ingham, M., Clilverd, M. A., Dalzell, M., Divett, T., et al. (2022). Geomagnetically induced current model in New Zealand across multiple disturbances: Validation and extension to non-monitored transformers. *Space Weather*, *20*(2), e2021SW002955. https://doi.org/10.1029/2021SW002955

Mac Manus, D. H., Rodger, C. J., Renton, A., Ronald, J., Harper, D., Taylor, C., et al. (2023). Geomagnetically induced current mitigation in New Zealand: Operational mitigation method development with industry input. *Space Weather*, *21*(11), e2023SW003533. https://doi.org/10.1029/2023SW003533

Madsen, F. D., Beggan, C. D., & Whaler, K. A. (2022). Forecasting changes of the magnetic field in the United Kingdom from L1 Lagrange solar wind measurements. *Frontiers in Physics*, *10*, 1091. https://doi.org/10.3389/FPHY.2022.1017781

Malone-Leigh, J., Campanyà, J., Gallagher, P. T., Neukirch, M., Hogg, C., & Hodgson, J. (2023). Nowcasting geoelectric fields in Ireland using magnetotelluric transfer functions. *Journal of Space Weather and Space Climate*, *13*(46), 6. https://doi.org/10.1051/SWSC/2023004

Marsal, S., & Torta, J. M. (2019). Quantifying the performance of geomagnetically induced current models. *Space Weather*, *17*(7), 941–949. https://doi.org/10.1029/2019SW002208

Marshall, R. A., Dalzell, M., Waters, C. L., Goldthorpe, P., & Smith, E. A. (2012). Geomagnetically induced currents in the New Zealand power network. *Space Weather*, *10*(8). https://doi.org/10.1029/2012SW000806

Marshall, R. A., Smith, E. A., Francis, M. J., Waters, C. L., & Sciffer, M. D. (2011). A preliminary risk assessment of the Australian region power network to space weather. *Space Weather*, *9*(10). https://doi.org/10.1029/2011SW000685

Marshall, R. A., Waters, C. L., & Sciffer, M. D. (2010). Spectral analysis of pipe-to-soil potentials with variations of the Earth's magnetic field in the Australian region. *Space Weather*, *8*(5). https://doi.org/10.1029/2009SW000553

McKinney, W. (2010). Data structures for statistical computing in python [Software]. Retrieved from http://conference.scipy.org/proceedings/scipy2010/mckinney.html

Milan, S. E., Bower, G. E., Fleetham, A. L., Imber, S. M., Schillings, A., Opgenoorth, H., et al. (2024). Occurrence and causes of large dB/dt events and AL bays in the pre-midnight and dawn sectors. *Journal of Geophysical Research: Space Physics*, *129*(10), e2024JA032811. https://doi.org/10.1029/2024JA032811

Milan, S. E., Clausen, L. B. N., Coxon, J. C., Carter, J. A., Walach, M.-T., Laundal, K., et al. (2017). Overview of solar wind–magnetosphere–ionosphere–atmosphere coupling and the generation of magnetospheric currents. *Space Science Reviews*, *206*(1–4), 547–573. https://doi.org/10.1007/s11214-017-0333-0

Milan, S. E., Imber, S. M., Fleetham, A. L., & Gjerloev, J. (2023). Solar cycle and solar wind dependence of the occurrence of large dB/dt events at high latitudes. *Journal of Geophysical Research: Space Physics*, *128*(4), e2022JA030953. https://doi.org/10.1029/2022JA030953

Molinski, T. S. (2002). Why utilities respect geomagnetically induced currents. *Journal of Atmospheric and Solar-Terrestrial Physics*, *64*(16), 1765–1778. https://doi.org/10.1016/S1364-6826(02)00126-8

Montiel-Álvarez, A. M., Hübert, J., Whaler, K., Beggan, C. D., Kiyan, D., & Hogg, C. (2025). The first three-dimensional electrical resistivity model of the lithosphere beneath Britain. *Journal of Geophysical Research: Solid Earth*, *130*(10), e2025JB031813. https://doi.org/10.1029/2025JB031813

Newell, P. T., & Gjerloev, J. W. (2011). Evaluation of SuperMAG auroral electrojet indices as indicators of substorms and auroral power. *Journal of Geophysical Research*, *116*(A12). https://doi.org/10.1029/2011JA016779

Newell, P. T., & Gjerloev, J. W. (2012). SuperMAG-based partial ring current indices. *Journal of Geophysical Research*, *117*(A5), 5215. https://doi.org/10.1029/2012JA017586

Ohtani, S. (2021). Revisiting the partial ring current model: Longitudinal asymmetry of ground magnetic depression during geomagnetic storms. *Journal of Geophysical Research: Space Physics*, *126*(9), e2021JA029643. https://doi.org/10.1029/2021JA029643

Ohtani, S. (2022). New insights from the 2003 Halloween storm into the Colaba 1600 nT magnetic depression during the 1859 Carrington storm. *Journal of Geophysical Research: Space Physics*, *127*(9), e2022JA030596. https://doi.org/10.1029/2022JA030596

Ohtani, S., Gjerloev, J. W., Anderson, B. J., Kataoka, R., Troshichev, O., & Watari, S. (2018). Dawnside wedge current system formed during intense geomagnetic storms. *Journal of Geophysical Research: Space Physics*, *123*(11), 9093–9109. https://doi.org/10.1029/2018JA025678

Oughton, E. J., Hapgood, M., Richardson, G. S., Beggan, C. D., Thomson, A. W., Gibbs, M., et al. (2019). A risk assessment framework for the socioeconomic impacts of electricity transmission infrastructure failure due to space weather: An application to the United Kingdom. *Risk Analysis*, *39*(5), 1022–1043. https://doi.org/10.1111/risa.13229

Oughton, E. J., Renton, A., Mac Marnus, D., Bor, D., & Rodger, C. J. (2025). Assessing the economic benefits of space weather mitigation investment decisions: Evidence from Aotearoa New Zealand. Retrieved from https://arxiv.org/abs/2507.12495v2

Papitashvili, N. E., & King, J. H. (2020). OMNI, combined solar wind plasma moments and interplanetary magnetic field (IMF) time-shifted to the nose of the Earth's bow shock, plus geomagnetic indices, 1 min data [Dataset]. *NASA Space Physics Data Facility*. https://doi.org/10.48322/mj0k-fq60

Parry, H. G., Cordell, D. R., Unsworth, M. J., MacMullin, R., & Mann, I. R. (2025). The influence of 3-D Earth conductivity, geoelectric field polarization, and power grid topology on GIC risk. *Space Weather*, *23*(11), e2025SW004544. https://doi.org/10.1029/2025SW004544

Partamies, N., Weygand, J. M., & Juusola, L. (2017). Statistical study of auroral omega bands. *Annales Geophysicae*, *35*(5), 1069–1083. https://doi.org/10.5194/ANGEO-35-1069-2017

Patterson, C. J., Wild, J. A., & Boteler, D. H. (2023). Modeling the impact of geomagnetically induced currents on electrified railway signaling systems in the United Kingdom. *Space Weather*, *21*(3), e2022SW003385. https://doi.org/10.1029/2022SW003385

Piersanti, M., Alberti, T., Bemporad, A., Berrilli, F., Bruno, R., Capparelli, V., et al. (2017). Comprehensive analysis of the geoeffective solar event of 21 June 2015: Effects on the magnetosphere, plasmasphere, and ionosphere systems. *Solar Physics*, *292*(11), 1–56. https://doi.org/10.1007/S11207-017-1186-0

Pinto, V. A., Keesee, A. M., Coughlan, M., Mukundan, R., Johnson, J. W., Ngwira, C. M., & Connor, H. K. (2022). Revisiting the ground magnetic field perturbations challenge: A machine learning perspective. *Frontiers in Astronomy and Space Sciences*, *9*, 123. https://doi.org/10.3389/fspas.2022.869740

Pratscher, K. M., Ingham, M., Manus, D. H. M., Kruglyakov, M., Heise, W., Rodger, C. J., et al. (2024). Modeling GIC in the Southern South Island of Aotearoa New Zealand using magnetotelluric data. *Space Weather*, *22*(7), e2024SW003907. https://doi.org/10.1029/2024SW003907

Pulkkinen, A., & Kataoka, R. (2006). S-transform view of geomagnetically induced currents during geomagnetic superstorms. *Geophysical Research Letters*, *33*(12). https://doi.org/10.1029/2006GL025822

Pulkkinen, A., Lindahl, S., Viljanen, A., & Pirjola, R. (2005). Geomagnetic storm of 29-31 October 2003: Geomagnetically induced currents and their relation to problems in the Swedish high-voltage power transmission system. *Space Weather*, *3*(8). https://doi.org/10.1029/2004SW000123

Reiff, P. H., Daou, A. G., Sazykin, S. Y., Nakamura, R., Hairston, M. R., Coffey, V., et al. (2016). Multispacecraft observations and modeling of the 22/23 June 2015 geomagnetic storm. *Geophysical Research Letters*, *43*(14), 7311–7318. https://doi.org/10.1002/2016GL069154

Rodger, C. J., Clilverd, M. A., Mac Manus, D. H., Martin, I., Dalzell, M., Brundell, J. B., et al. (2020). Geomagnetically induced currents and harmonic distortion: Storm-time observations from New Zealand. *Space Weather*, *18*(3), e2019SW002387. https://doi.org/10.1029/2019SW002387

Rodger, C. J., Mac Manus, D. H., Dalzell, M., Thomson, A. W. P., Clarke, E., Petersen, T., et al. (2017). Long-Term geomagnetically induced current observations from New Zealand: Peak current estimates for extreme geomagnetic storms. *Space Weather*, *15*(11), 1447–1460. https://doi.org/10.1002/2017SW001691

Rogers, N. C., Wild, J. A., Eastoe, E. F., Gjerloev, J. W., & Thomson, A. W. P. (2020). A global climatological model of extreme geomagnetic field fluctuations. *Journal of Space Weather and Space Climate*, *10*, 5. https://doi.org/10.1051/swsc/2020008

Rogers, N. C., Wild, J. A., Eastoe, E. F., & Hübert, J. (2021). Climatological statistics of extreme geomagnetic fluctuations with periods from 1 s to 60 min. *Space Weather*, *19*(11), e2021SW002824. https://doi.org/10.1029/2021SW002824

Rosenqvist, L., Fristedt, T., Dimmock, A. P., Davidsson, P., Fridström, R., Hall, J. O., et al. (2022). 3D modeling of geomagnetically induced currents in Sweden—Validation and extreme event analysis. *Space Weather*, *20*(3), e2021SW002988. https://doi.org/10.1029/2021SW002988

Rosenqvist, L., Johlander, A., Molenkamp, S., Dimmock, A. P., Setréus, J., & Lanabere, V. (2025). A novel approach for evaluating GIC impacts in the Swedish power grid. *Space Weather*, *23*(6), e2024SW004313. https://doi.org/10.1029/2024SW004313

Schillings, A., Palin, L., Opgenoorth, H. J., Hamrin, M., Rosenqvist, L., Gjerloev, J., et al. (2022). Distribution and occurrence frequency of dB/dt spikes during magnetic storms 1980 - 2020. *Space Weather*, *20*(5), e2021SW002953. https://doi.org/10.1029/2021SW002953

Schrijver, C. J., Dobbins, R., Murtagh, W., & Petrinec, S. M. (2014). Assessing the impact of space weather on the electric power grid based on insurance claims for industrial electrical equipment. *Space Weather*, *12*(7), 487–498. https://doi.org/10.1002/2014SW001066

Shim, J. S., Kuznetsova, M., Rastätter, L., Hesse, M., Bilitza, D., Butala, M., et al. (2011). CEDAR electrodynamics thermosphere ionosphere (ETI) challenge for systematic assessment of ionosphere/thermosphere models: NmF2, hmF2, and vertical drift using ground-based observations. *Space Weather*, *9*(12), 12003. https://doi.org/10.1029/2011SW000727

Siciliano, F., Consolini, G., Tozzi, R., Gentili, M., Giannattasio, F., & De Michelis, P. (2020). Forecasting SYM-H index: A comparison between long short-term memory and convolutional neural networks. *Space Weather*, *19*(2), e2020SW002589. https://doi.org/10.1029/2020SW002589

Smith, A. J., Freeman, M. P., Hunter, S., & Milling, D. K. (2002). VLF, magnetic bay, and Pi2 substorm signatures at auroral and midlatitude ground stations. *Journal of Geophysical Research*, *107*(A12), SM14–1–SMP14–14. https://doi.org/10.1029/2002JA009389

Smith, A. W., Forsyth, C., Rae, I. J., Garton, T. M., Bloch, T., Jackman, C. M., & Bakrania, M. (2021). Forecasting the probability of large rates of change of the geomagnetic field in the UK: Timescales, Horizons and thresholds. *Space Weather*, *19*(9), e2021SW002788. https://doi.org/10.1029/2021SW002788

Smith, A. W., Forsyth, C., Rae, J., Rodger, C. J., & Freeman, M. P. (2021). The impact of sudden commencements on ground magnetic field variability: Immediate and delayed consequences. *Space Weather*, *19*(7), e2021SW002764. https://doi.org/10.1029/2021SW002764

Smith, A. W., Freeman, M. P., Rae, I. J., & Forsyth, C. (2019). The influence of sudden commencements on the rate of change of the surface horizontal magnetic field in the United Kingdom. *Space Weather*, *17*(11), 1605–1617. https://doi.org/10.1029/2019SW002281

Smith, A. W., Rodger, C. J., Mac Manus, D. H., Rae, I. J., Fogg, A. R., Forsyth, C., et al. (2024). Sudden commencements and geomagnetically induced currents in New Zealand: Correlations and dependance. *Space Weather*, *22*(1), e2023SW003731. https://doi.org/10.1029/2023SW003731

Smith, A. W., Rodger, C. J., Mac Manus, D. H., Forsyth, C., Rae, I. J., Freeman, M. P., et al. (2022). The correspondence between sudden commencements and geomagnetically induced currents: Insights from New Zealand. *Space Weather*, *20*(8), e2021SW002983. https://doi.org/10.1029/2021SW002983

Smith, A. W., Rodger, C. J., Pratscher, K. M., Mac Manus, D. H., Rae, I. J., Ratliff, D., et al. (2025). Why do sudden commencements sometimes generate disproportionate geomagnetically induced currents? *Space Weather*, *23*(10), e2025SW004533. https://doi.org/10.1029/2025SW004533

Thomson, A. W., Dawson, E. B., & Reay, S. J. (2011). Quantifying extreme behavior in geomagnetic activity. *Space Weather*, *9*(10). https://doi.org/10.1029/2011SW000696

Upendran, V., Tigas, P., Ferdousi, B., Bloch, T., Cheung, M. C. M., Ganju, S., et al. (2022). Global geomagnetic perturbation forecasting using deep learning. *Space Weather*, *20*(6), e2022SW003045. https://doi.org/10.1029/2022SW003045

Van Der Walt, S., Colbert, S. C., & Varoquaux, G. (2011). The NumPy array: A structure for efficient numerical computation [Software]. *Computing in Science & Engineering*, *13*(2), 22–30. https://doi.org/10.1109/MCSE.2011.37

Vasseur, G., & Weidelt, P. (1977). Bimodal electromagnetic induction in non-uniform thin sheets with an application to the northern Pyrenean induction anomaly. *Geophysical Journal International*, *51*(3), 669–690. https://doi.org/10.1111/J.1365-246X.1977.TB04213.X

Viljanen, A., Nevanlinna, H., Pajunpää, K., & Pulkkinen, A. (2001). Time derivative of the horizontal geomagnetic field as an activity indicator. *Annales Geophysicae*, *19*(9), 1107–1118. https://doi.org/10.5194/angeo-19-1107-2001

Virtanen, P., Gommers, R., Oliphant, T. E., Haberland, M., Reddy, T., Cournapeau, D., et al. (2020). SciPy 1.0: Fundamental algorithms for scientific computing in python [Software]. *Nature Methods*, *17*(3), 261–272. https://doi.org/10.1038/s41592-019-0686-2

Walach, M.-T., & Milan, S. E. (2015). Are steady magnetospheric convection events prolonged substorms? *Journal of Geophysical Research: Space Physics*, *120*(3), 1751–1758. https://doi.org/10.1002/2014JA020631

Walach, M.-T., Milan, S. E., Murphy, K. R., Carter, J. A., Hubert, B. A., & Grocott, A. (2017). Comparative study of large-scale auroral signatures of substorms, steady magnetospheric convection events, and sawtooth events. *Journal of Geophysical Research: Space Physics*, *122*(6), 6357–6373. https://doi.org/10.1002/2017JA023991

Wallner, A. V. L., Dimmock, A. P., Lanabere, V., Johlander, A., Venholen, S. M., Viljanen, A., et al. (2026). The geomagnetic storm on 10–12 May 2024 and its effect on the Swedish power grid. *Space Weather*, *24*(2), e2025SW004788. https://doi.org/10.1029/2025SW004788

Walsh, A. P., Haaland, S., Forsyth, C., Keesee, A. M., Kissinger, J., Li, K., et al. (2014). Dawn-dusk asymmetries in the coupled solar wind-magnetosphere-ionosphere system: A review. *Annales Geophysicae*, *32*(7), 705–737. https://doi.org/10.5194/angeo-32-705-2014

Wang, T., Fletcher, D., Parry, M., Rodger, C. J., Smith, A. W., & Petersen, T. (2025). Better forecasting of extreme geomagnetic storms using non-stationary statistical models. *Space Weather*, *23*(7), e2025SW004404. https://doi.org/10.1029/2025SW004404

Waters, C. L., Anderson, B. J., Green, D. L., Korth, H., Barnes, R. J., & Vanhamäki, H. (2020). Science data products for AMPERE. *Ionospheric Multi-Spacecraft Analysis Tools*, 141–165. https://doi.org/10.1007/978-3-030-26732-2_7

Waters, C. L., Anderson, B. J., & Liou, K. (2001). Estimation of global field aligned currents using the iridium® system magnetometer data. *Geophysical Research Letters*, *28*(11), 2165–2168. https://doi.org/10.1029/2000GL012725

Waters, C. L., & Marshall, R. A. (2026). The relationship between the magnetometer data derived GIC index and measured GIC in high voltage transformers in Australia. *Space Weather*, *24*(1), e2025SW004665. https://doi.org/10.1029/2025SW004665

Wild, J. A., Yeoman, T. K., Eglitis, P., & Opgenoorth, H. J. (2000). Multi-instrument observations of the electric and magnetic field structure of omega bands. *Annales Geophysicae*, *18*(1), 99–110. https://doi.org/10.1007/S00585-000-0099-6

Zois, I. P. (2013). Solar activity and transformer failures in the Greek national electric grid. *Journal of Space Weather and Space Climate*, *3*, A32. https://doi.org/10.1051/SWSC/2013055

Zou, Y., Dowell, C., Ferdousi, B., Lyons, L. R., & Liu, J. (2022). Auroral drivers of large dB/dt during geomagnetic storms. *Space Weather*, *20*(11), e2022SW003121. https://doi.org/10.1029/2022SW003121